Wiley Analytical Science

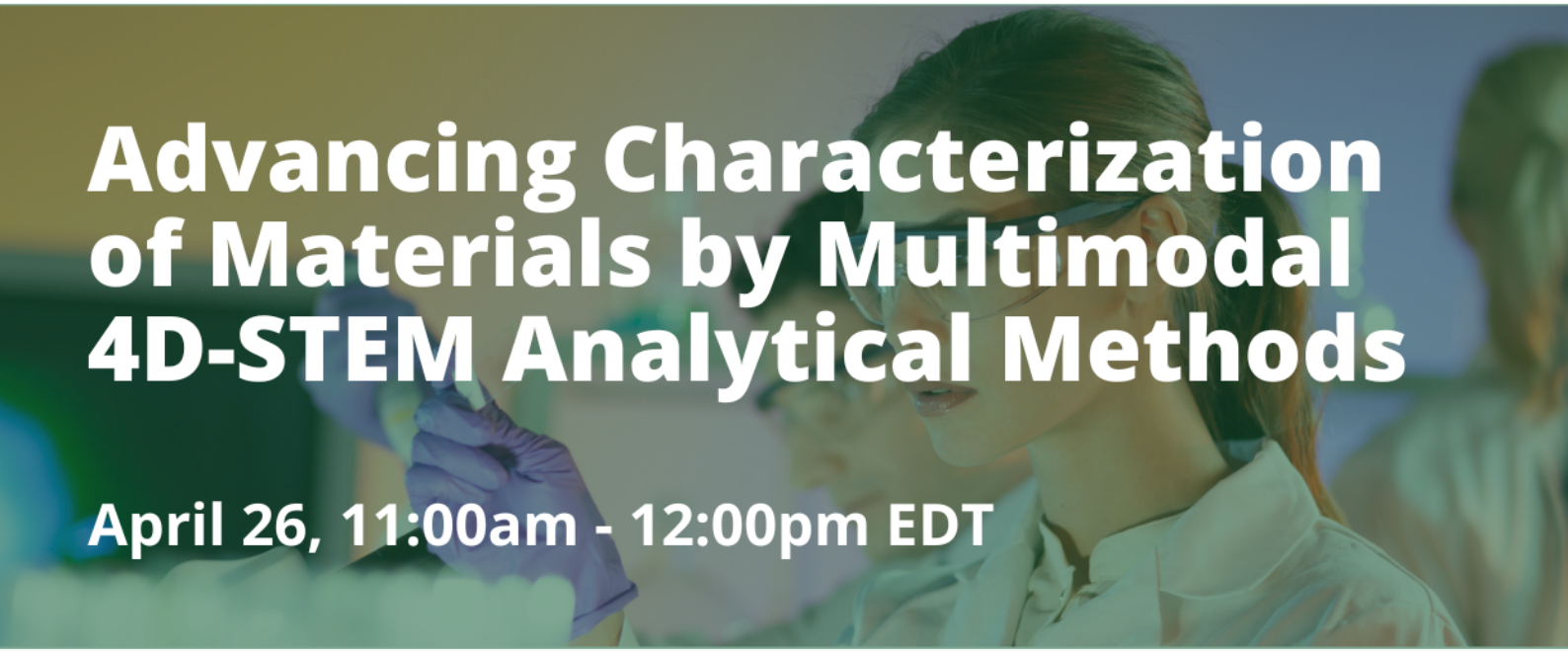

Advancing Characterization of Materials by Multimodal 4D-STEM Analytical Methods

April 26, 11:00am - 12:00pm EDT

Development and production of new materials and semiconductor devices require morphological, structural, and chemical characterization at the nanoscale level to understand their chemico-physical properties and optimize their production process. Besides traditional electron microscopy imaging and compositional analysis techniques, 4D-STEM methods provide additional structural information about the local internal organization of atoms and molecules at each position of an acquired STEM map.

Watch this session during the WAS Virtual Conference:

Dr. Daniel Nemecek

Dr. Tingting Yang

Register Now

This talk is sponsored by TESCAN
PERFORMANCE IN NANOSPACE

ADVANCED OPTICAL MATERIALS
www.advopticalmat.de

Laser-Driven Strong-Field Terahertz Sources

József András Fülöp, Stelios Tzortzakis, and Tobias Kampfrath*

A review on the recent development of intense laser-driven terahertz (THz) sources is provided here. The technologies discussed include various types of sources based on optical rectification (OR), spintronic emitters, and laser-filament-induced plasma. The emphasis is on OR using pump pulses with tilted intensity front. Illustrative examples of newly emerging applications are briefly discussed, in particular strong-field THz control of materials and acceleration and manipulation of charged particles.

1. Introduction

Over the past decades, electromagnetic radiation in the terahertz (THz) frequency range from ≈1 to ≈30 THz (1 THz = 10^{12} Hz) has been attracting a constantly increasing interest as a powerful probe in spectroscopy, materials science, and imaging.[1,2] A major reason for this interest relies on the fact that THz radiation can couple resonantly to numerous fundamental motions of ions, electrons, and electron spins in all phases of matter. For example, in solids, the THz range overlaps with the frequency of lattice vibrations (phonons), the collision rates of conduction electrons, the binding energy of bound electron–hole pairs (excitons), and the precession frequency of spin waves (magnons). Consequently, THz radiation, both continuous-wave and pulsed, has been used for characterization of and gaining insight into elementary processes in complex materials. The majority of these studies used relatively weak THz fields and, thus, probed the linear response of the material, without inducing notable material modifications.

Only recently, however, completely new avenues in THz science were opened up by triggering nonlinear THz responses of materials.[3–13] Instead of using weak fields to primarily observe selected THz modes such as phonons or magnons, strong fields allow one to actively drive them to unprecedentedly large amplitudes, potentially thereby resulting in novel states of matter.[6,8,11] For example, simulations suggest that exciting matter with intense THz transients may lead to massive modifications of electrically[14] or magnetically[15] ordered domains and enable the acceleration of free ions to ≈1 MeV,[16] and postacceleration to 50–100 MeV energies.[17] Remarkable experimental results such as switching of magnetic order,[18,19] parametric amplification of optical phonons,[20] novel insights into spin-lattice coupling,[21,22] and acceleration of free electrons in a THz linear accelerator[23] were achieved only recently.

This progress has been made possible by the development of laser-driven table-top THz sources routinely providing pulses with unprecedented energies and peak electric and magnetic field strengths throughout the entire THz spectral range. Different laser-based THz pulse generation techniques can be used to access different parts of the spectral range extending from 0.1 to 10 THz. Some of the recently developed technologies enable the generation of radiation with even larger bandwidth or tuning range up to 100 THz and beyond, which lead to an extension of what is called the THz spectral range. An overview of the approximate spectral coverage and the achieved highest pulse energies and peak electric-field strengths of various laser-driven technologies is given in **Figure 1**.

1.1. Scope

In this work, the basic principles of femtosecond-laser-driven intense pulsed THz sources and their recent development are reviewed. These sources are capable of delivering peak electric field strengths on the MV cm^{-1} scale. Corresponding typical THz pulse energies are on the μJ-to-mJ level, depending on

Dr. J. A. Fülöp
MTA-PTE High-Field Terahertz Research Group
7624 Pécs, Hungary
E-mail: fulop@fizika.ttk.pte.hu
Dr. J. A. Fülöp
ELI-ALPS
ELI-HU Nonprofit Ltd.
6720 Szeged, Hungary
Dr. J. A. Fülöp
Szentágothai Research Centre
University of Pécs
7624 Pécs, Hungary
Prof. S. Tzortzakis
Science Program
Texas A&M University at Qatar
P.O. Box 23874, Doha, Qatar
Prof. S. Tzortzakis
Materials Science and Technology Department
University of Crete
71003 Heraklion, Greece
Prof. S. Tzortzakis
Institute of Electronic Structure and Laser
Foundation for Research and Technology Hellas
71110 Heraklion, Greece
Prof. T. Kampfrath
Department of Physics
Freie Universität Berlin
14195 Berlin, Germany
Prof. T. Kampfrath
Department of Physical Chemistry
Fritz Haber Institute of the Max Planck Society
14195 Berlin, Germany
The ORCID identification number(s) for the author(s) of this article can be found under https://doi.org/10.1002/adom.201900681.

DOI: 10.1002/adom.201900681

frequency. In Section 2, THz sources based on optical rectification (OR) are discussed. The emphasis in this Review is on approaches using tilted pump intensity fronts, because the efficient lithium-niobate-based tilted-pulse-front technique has found a very widespread use in nonlinear THz spectroscopy today and, because exciting new perspectives have been opened up by recent progress. Section 3 deals with solid-state THz sources relying on photocurrents driven by absorbed optical light, with emphasis on the newly emerging spintronic THz emitters (STEs). In Section 4, THz sources based on laser-filament-induced plasmas are considered, emphasizing the perspectives of infrared driver pulses. Finally, in Section 5, selected application examples from nonlinear THz spectroscopy and control of materials by intense THz pulses are briefly discussed.

1.2. Basic Principles of Laser-Based Generation of THz Radiation

To generate an electromagnetic wave with frequency $\Omega/2\pi$, an electrical source current distribution $\mathbf{j}_{\mathrm{THz}}$ oscillating at the same frequency is required. A fundamental example is a Hertzian dipole whose temporally oscillating current density is spatially localized in a subwavelength volume (**Figure 2**a). In a homogenous medium, the Hertzian dipole is known to emit an electromagnetic wave which features the typical spherical phase fronts (Figure 2a) and dipolar directional characteristics in the far-field.[24]

Oscillating, and more generally, time-dependent currents can be generated, e.g., by the flow of quasi-free electrons in metals and semiconductors, the displacement of the charge density of bound electrons in insulators and the vibrations of lattice ions. One often writes the current density $\mathbf{j}_{\mathrm{THz}} = \partial \mathbf{P}_{\mathrm{THz}}/\partial t$ as time-derivative of the so-called polarization $\mathbf{P}_{\mathrm{THz}}$, which can, up to a certain extent,[25] be interpreted as the induced dipole moment per volume.

As optical radiation has frequencies on the order of several 100 THz, it only generates a THz-frequency polarization or current if a *nonlinear response* is involved.[26] In the simplest case, this induced polarization or current scales with the square of the driving optical field. Important examples are OR (in optically transparent media) or photocurrents (involving single-photon absorption of light). In electric-dipole approximation, such a quadratic optical response is restricted to materials and structures lacking inversion symmetry.

Note that the driving optical field is often spatially extended, resulting in a possibly complex spatiotemporal distribution of $\mathbf{j}_{\mathrm{THz}}$. To obtain a sizeable field amplitude in a beam-like output, the spherical waves emitted from all locations of $\mathbf{j}_{\mathrm{THz}}$ need to superimpose constructively in a particular direction.[24] This *phase matching* condition is not easy to fulfil, e.g., in the case of OR in bulk crystals (see Section 2), because optical and THz waves usually have different propagation velocities in materials.

An illustrative example is that of a focused optical pulse propagating through the nonlinear optical material $LiNbO_3$ (Figure 2b; see also Section 2.2). At each position along its path, the optical pulse creates, through OR, a local polarization oscillating at frequency $\Omega/2\pi$. Note that this situation of a moving Hertzian dipole (Figure 2b) is more complex than that of a single Hertzian dipole at rest (Figure 2a), since the moving dipole generates not just one but a whole series of temporally and spatially shifted spherical waves along its path. Because in $LiNbO_3$ the THz phase velocity is lower than the group velocity of the optical pulse, the spherical waves starting from each point of the optical path superimpose constructively only on the surface of a cone.[4,27,28] This situation is disadvantageous

József András Fülöp obtained his Ph.D. degree in 2003 from University of Szeged (Hungary) and then worked as a postdoctoral researcher at the Ludwig-Maximilans-Universität in Munich (Germany). In 2007, he joined the University of Pécs (Hungary) and in 2010 ELI-ALPS in Szeged (Hungary), where he is leading the THz Group. Since 2019 he is a scientific adviser at the MTA-PTE High-Field Terahertz Research Group in Pécs. He is working on the development of intense THz sources and their applications.

Stelios Tzortzakis received his Ph.D. in 2001 from the Ecole Polytechnique (France). He is full professor of physics at Texas A&M University at Qatar (since 2015), associate professor at the Materials Department of the University of Crete (Greece; since 2011), and collaborating faculty at the Institute of Electronic Structure and Laser (IESL-FORTH, Greece; since 2006), where he was deputy director for 9 years. His expertise is on nonlinear propagation of high-power lasers and nonlinear THz science.

Tobias Kampfrath obtained his Ph.D. degree from the Freie Universität Berlin (Germany) in 2006 and then worked as postdoctoral fellow at AMOLF Amsterdam (Netherlands). In 2010, he became head of the Terahertz Physics Group at the Fritz Haber Institute of the Max Planck Society in Berlin (Germany). Since 2017, he is full professor at the Department of Physics of the Freie Universität Berlin, working on terahertz dynamics of condensed matter, in particular magnetic nanostructures.

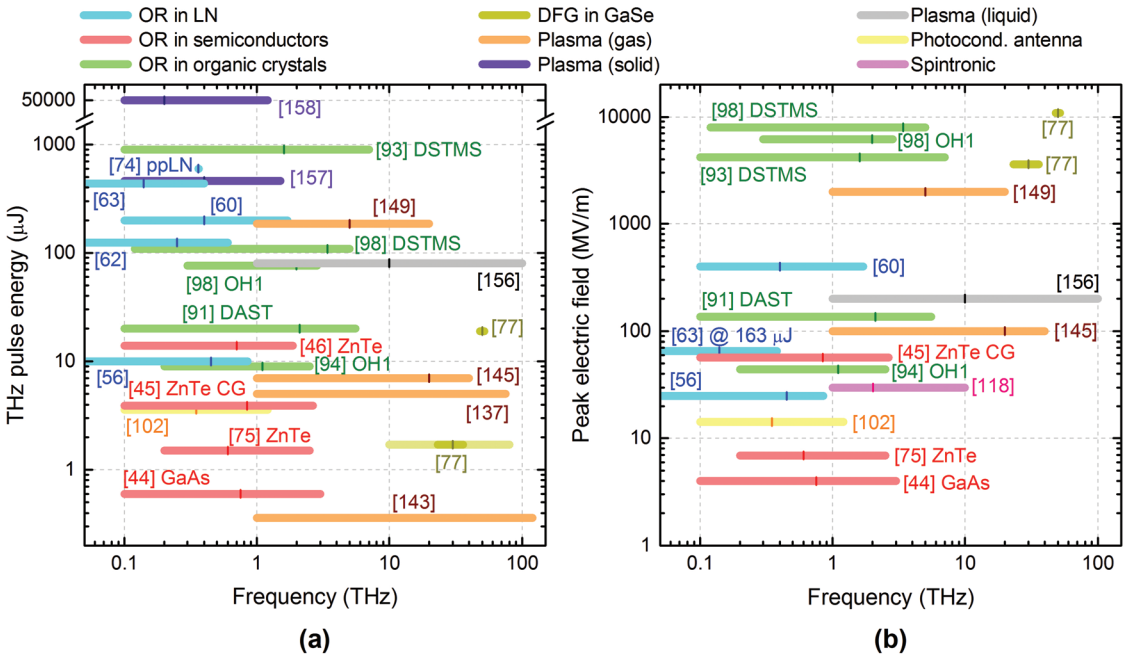

Figure 1. Approximate spectral coverage and some of the highest reported experimental values of a) THz pulse energy and b) peak electric field strength for various types of laser-driven pulsed THz sources. The spectral coverage refers to the width at 10% of the peak amplitude. The short vertical lines indicate the approximate frequencies of the spectral peaks. OR: optical rectification, LN: $LiNbO_3$, DFG: difference-frequency generation, CG: contact grating.

for most applications and makes it plausible that for laterally extended beams, constructive superposition (phase matching) is only obtained for appropriately tailored spatio-temporal distributions of the optical pulse (see Section 2.1).

The above considerations show that efficient generation of THz radiation requires media or structures with strong nonlinear optical response and the possibility of phase matching, ideally over large optical and THz bandwidths.

It is worth mentioning that Wynne and Carey gave an integrated 1D description of THz generation driven by a laser pulse travelling through the medium and inducing a polarization oscillating at THz frequencies.[29] This description is valid for various mechanisms, such as OR, microscopic currents from photoinduced charge transfer in aligned molecules, and current surge (photoconductive antennas). In the simplest case of an instantaneously responding medium, vanishing dispersion in the THz range, and perfect phase matching, the electric field of the THz pulse is shaped, for an extended source, according to the time derivative of the intensity envelope of the optical pulse. Remarkably, the generated THz pulses exhibit a fixed carrier-envelope phase and, for Gaussian-like pump envelopes, single-cycle-type waveforms. These features are essential for many field-driven applications.

2. THz Sources based on OR

The generation of THz radiation in electro-optical materials was investigated as early as 1971.[30,31] Generation of nearly single-cycle THz pulses by OR was first demonstrated by Auston et al. in 1984.[28]

OR, a second-order nonlinear optical process, is a special case of difference-frequency generation (DFG)[26] and can be driven by a femtosecond optical pulse. Spectral components with angular frequencies ω and $\omega + \Omega$ from the optical pulse are mixed by DFG, thereby generating a new spectral component with angular frequency Ω in the THz range (**Figure 3**). Thus, OR can be described as intrapulse DFG, as opposed to interpulse DFG with two input pulses of possibly different carrier frequencies. Phenomenologically, the nonlinear polarization induced by the pump pulse can be calculated as[26,32]

$$P_{\mathrm{NL}}(\Omega) = 2\varepsilon_0 \int_0^\infty d_{\mathrm{eff}} E(\omega+\Omega) E^*(\omega)\,\mathrm{d}\omega \tag{1}$$

where ε_0 is the permittivity of free space, $E(\omega)$ is the one-sided ($\omega > 0$) Fourier-component of the pump pulse at optical angular frequency ω, and Ω is the difference frequency. The effective second-order nonlinear coefficient of the medium d_{eff} is, in general, dependent on the frequencies ω and Ω.[26] Typical optical pump pulse durations used for OR range from about 30 fs to 1.5 ps. Therefore, the generated difference-frequency spectral components lie in the THz range. According to Equation (1), a narrowband pump pulse generates low THz frequencies, whereas a broadband pulse can generate a broad THz spectrum containing also higher THz frequencies. Note that the complex conjugate E^* in Equation (1) makes the resulting polarization independent of the carrier-envelope phase of the driving optical field, resulting in a carrier-envelope phase stable THz pulse, as already mentioned above.

The build-up of the THz field over macroscopic distances in the medium is described by the inhomogenous wave equation.[26] Besides the nonlinear polarization, this process is

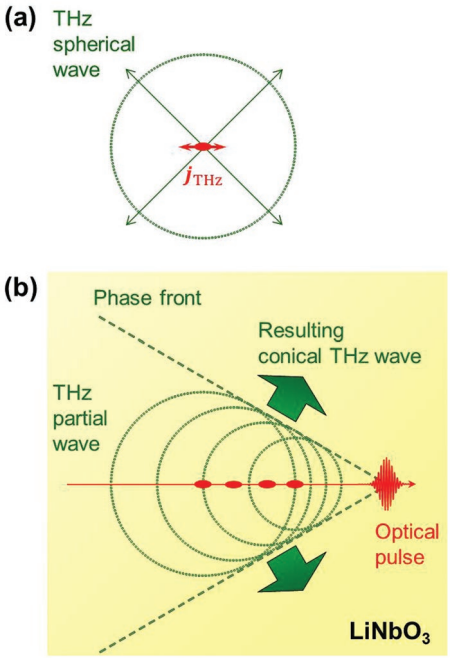

Figure 2. General idea of laser-based THz-pulse generation. a) A localized current density oscillating at a THz frequency (Hertzian dipole) emits an electromagnetic wave with spherical phase fronts. b) A focused laser pulse propagates through the transparent nonlinear optical crystal $LiNbO_3$. The elementary spherical THz waves superimpose constructively on the surface of a cone.

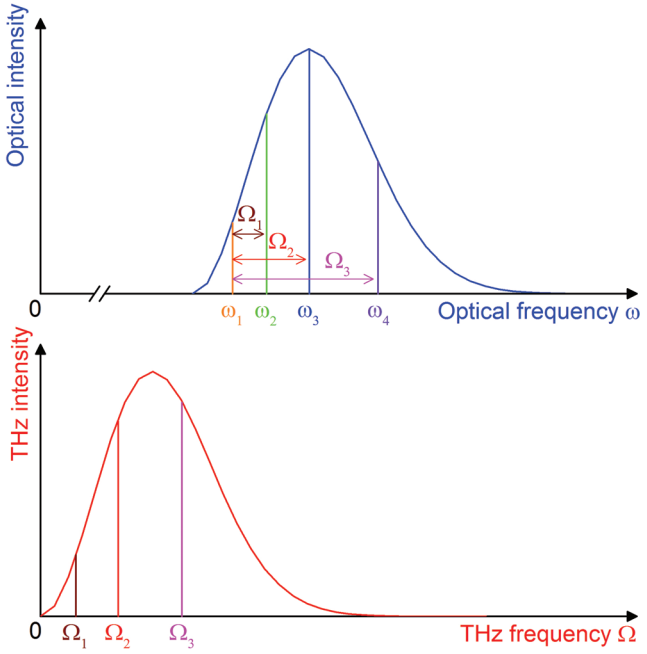

Figure 3. Schematic representation of optical and THz spectra in case of OR. Each pair of optical frequency components (upper panel) generates a THz spectral component at their difference frequency (lower panel).

also influenced by the dispersion of the medium. The efficiency of OR is highest when the phase-matching condition $\Delta k = 0$ is fulfilled between the pump and the THz fields,[26,32,33] where,

$$\Delta\mathbf{k} = \mathbf{k}(\Omega) + \mathbf{k}(\omega) - \mathbf{k}(\omega + \Omega) \approx \mathbf{k}(\Omega) - \left.\frac{\partial \mathbf{k}}{\partial \omega}\right|_{\omega_0} \cdot \Omega \tag{2}$$

The second, approximate equality holds if $\Omega \ll \omega$, which is usually valid for THz generation by OR. For collinear phase matching, Equation (2) gives $\Delta k = |\Delta\mathbf{k}| = [n(\Omega) - n_g(\omega_0)] \cdot \Omega/c$, where ω_0 is the pump central (carrier) frequency, c is the speed of light in vacuum, and n and n_g are the refractive and group indices, respectively. Thus, in the case of phase-matched propagation, the phase velocity $v = c/n$ of the generated THz radiation equals the group velocity $v_g = c/n_g$ of the optical pump pulse, and the velocity-matching condition

$$v(\Omega) = v_g(\omega_0) \tag{3}$$

holds. Materials suitable for OR are semiconductors such as CdTe, GaAs, GaP, GaSe, or ZnTe, ferroelectric materials such as lithium niobate ($LiNbO_3$) or lithium tantalate ($LiTaO_3$), and organic materials such as 4-N,N-dimethylamino-4′-N′-methyl stilbazolium tosylate (DAST), 2-[3-(4-hydroxystyryl)-5.5-dimethylcyclohex-2-enylidene]malononitrile (OH1), 4-N, N-dimethylamino-4′-N′-methyl-stilbazolium 2,4,6-trimethylbenzenesulfonate (DSTMS), or 2-(4-hydroxy-3-methoxystyryl)-1-methylquinolinium 2,4,6-trimethylbenzenesulfonate (HMQ-TMS) (see Section 2.4). A detailed comparison of their properties can be found in Refs. [4,34–38]. For the selection of a suitable material, it is instructive to consider the expression for the THz generation efficiency in the case of phase matching[33]

$$\eta(\Omega) = \frac{2\Omega^2 d_{\text{eff}}^2 I^2 I}{\varepsilon_0 c^3 n^2(\omega_0) n(\Omega)} \cdot e^{-\alpha(\Omega)L/2} \cdot \frac{\sinh^2\left[\alpha(\Omega)L/4\right]}{\left[\alpha(\Omega)L/4\right]^2} \tag{4}$$

Here, L is the material length and I is the pump intensity. Obviously, a large effective nonlinear coefficient d_{eff} and a small THz absorption coefficient $\alpha(\Omega)$ are advantageous for a high efficiency. The scaling of η with the square of the THz frequency implies significantly higher efficiencies at higher THz frequencies and makes it challenging to achieve comparable values at low THz frequencies.

In a realistic model of intense THz sources, effects other than OR have to be taken into account. It is important to consider linear absorption in the THz range, determined by the complex dielectric function of the material. Absorption of pump light, especially multiphoton absorption (MPA), can cause an increased carrier concentration and absorption in the THz range.[37,39] In the case of very strong THz fields, it is important to take into account the influence of the generated THz pulse on the optical pump pulse, which is caused by their nonlinear interaction (such as sum- and difference-frequency generation between optical and THz fields).[40–42] At high pump intensities, additional nonlinear effects may occur, for instance self-phase modulation, second- and third-harmonic generation, or stimulated Raman scattering. In noncollinear geometries, spatio-temporal coupling can lead to additional complexity.

Below, an important phase-matching method, the tilted-pulse-front technique, is discussed first (Section 2.1). It is followed by the discussion of THz generation by OR in lithium niobate (Section 2.2), semiconductor (Section 2.3), and organic

crystals (Section 2.4), outlining specific features and state-of-the-art THz pulse parameters.

2.1. Tilted-Pulse-Front Pumping

The phase-matching condition, given by Equation (3), can be fulfilled in some cases, e.g., in GaSe, by utilizing the natural birefringence of the nonlinear material. Other semiconductors, such as ZnTe, GaP, or GaAs, are optically isotropic. Thus, collinear phase matching is possible only in specific cases, at particular pump and THz frequencies. A prominent example is ZnTe pumped at a wavelength of 0.8 μm to generate radiation around 1 THz frequency. At other wavelengths or in other materials, a specific noncollinear geometry, called tilted-pulse-front pumping (TPFP), may be used for phase matching.

The TPFP technique was proposed by Hebling et al. to enable efficient THz pulse generation in lithium niobate,[43] a material with high effective nonlinear coefficient but lack of collinear phase matching possibility for OR. Recently, it has also been applied to semiconductors.[39,44–46] TPFP is of great practical importance, as it is scalable to high THz pulse energies by simply increasing the pumped area. It enables broadband (achromatic) phase matching for OR in a noncollinear geometry involving pump angular dispersion using pump pulses with tilted intensity front.[4,43,47]

The scheme of TPFP is shown in **Figure 4**a. The pump pulse propagates with a tilted intensity front inside the nonlinear medium. The tilt angle of the pulse front with respect to the phase fronts is γ. The THz radiation is generated by the induced polarization along the tilted pulse front. Therefore, according to Huygens' principle, the THz radiation propagates perpendicularly to the pump pulse front. A strong THz field can build up if the source (the induced polarization along the pump pulse front), moving with the optical group velocity $v_g(\omega_0)$, remains in phase with the THz field, propagating with the phase velocity $v(\Omega)$. According to Figure 4a, this condition is fulfilled at the pulse-front tilt (PFT) angle γ satisfying the following more general form of the velocity matching condition of Equation (3)

$$v(\Omega) = v_g(\omega_0) \cdot \cos\gamma \tag{5}$$

This equation states that the projected pump group velocity needs to match the THz phase velocity. As the pump pulse propagates, it slides along the THz phase front. Obviously, Equation (5) can only be fulfilled in materials where the THz phase velocity is smaller than or equal to the pump group velocity.

The TPFP scheme can alternatively be described with wave vectors as noncollinear vector phase matching (Figure 4b). The PFT is linked to angular dispersion according to the relation[43,47,48]

$$\tan\gamma = -\frac{n}{n_g}\lambda\frac{\partial\varepsilon}{\partial\lambda} \tag{6}$$

The propagation angles $\varepsilon(\omega)$ with respect to the beam propagation direction z are typically small and for the z-projection of the wave vectors in case of phase matching $k(\Omega)\cos\gamma \approx k(\omega_0+\Omega) - k(\omega_0) \approx \Omega(\partial k/\partial\omega)|_{\omega_0}$ is a good approximation. By using the definitions of the wave vector and the phase and group velocities, one can easily obtain from this relation the velocity-matching condition of Equation (5).

The angular dispersion, present in TPFP schemes, contributes to the group-velocity dispersion,[47] in addition to the contribution from material dispersion. The group-velocity dispersion parameter can be written as[48,49]

$$D = \frac{\partial\left(v_g^{-1}\right)}{\partial\lambda} = \frac{\lambda}{c}\left[n\left(\frac{\partial\varepsilon}{\partial\lambda}\right)^2 - \frac{\partial^2 n}{\partial\lambda^2}\right] \tag{7}$$

where the first and second terms originate from angular dispersion and material dispersion, respectively. For a large PFT angle, the former can dominate over the latter, thereby significantly enhancing the variation of the pump pulse duration with propagation distance.[50] The influence of group-velocity dispersion, originating from angular dispersion, on THz generation will be discussed below for lithium niobate (Section 2.2).

2.2. Lithium Niobate

2.2.1. Basic Properties

Lithium niobate ($LiNbO_3$, LN) is one of the most widely used materials in intense THz sources nowadays. Its properties, relevant for THz generation by OR, can be found in Refs. [4,34–37,51,52]. The most important features can be summarized as follows:

- LN has a high effective nonlinear coefficient of $d_{eff} = d_{33} = 168$ pm V^{-1}. This value is higher than typical values for semiconductors, which range from about 25 to 80 pm V^{-1}, but smaller than that of organic materials. In order to utilize d_{33}, both the pump and the THz wave should be polarized along the dielectric Z axis of LN.

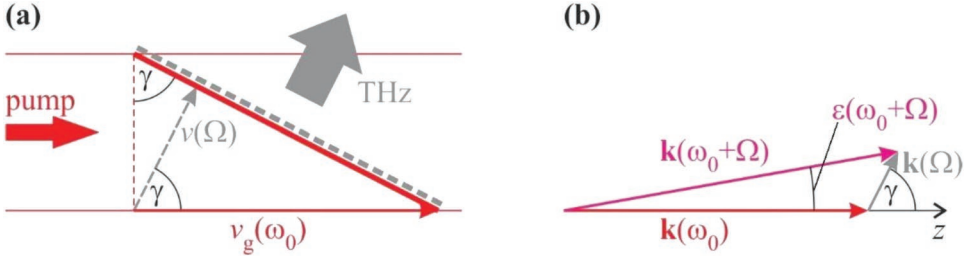

Figure 4. a) Scheme of TPFP with pump pulse front (thick red solid line) and THz phase front (thick gray dashed line). b) Noncollinear phase matching in TPFP. Reproduced with permission.[4] Copyright 2011, IOP Publishing.

- The THz absorption coefficient is relatively high (17 cm^{-1} at 1 THz) at room temperature, but can be significantly reduced (below 5 cm^{-1}) by cooling the crystal to cryogenic temperatures.[51] Phonon absorption limits the useful THz spectral range to the low-frequency part (up to about 4.5 THz[35]) of the THz spectrum.
- Although LN is optically anisotropic, utilizing birefringence for phase matching by angle tuning in OR is not possible below the transverse-optical phonon frequency, due to the strong contribution of the lattice vibration to the dielectric function.[35] Owing to the very different optical group and THz phase velocities, a large PFT angle γ of about 63° is required for phase matching.
- LN is available in congruent (cLN) and stoichiometric (sLN) forms, where somewhat higher THz generation efficiencies were achieved with the latter. Both types are available in large sizes up to several cm. To prevent photorefractive damage, the strong photorefractive effect can be significantly reduced by doping with MgO. The optimal doping concentration was found to be about 0.7% for sLN and 6% for cLN.[53]
- LN can be pumped at high intensities (≈100 GW cm^{-2}) owing to its high damage threshold. MPA of the pump usually plays a minor role as the material is an insulator with a large bandgap of 3.8 eV. At the typical pump wavelengths of 0.8 and 1.03 µm, the lowest-order effective MPA process is three-photon absorption (3PA) and four-photon absorption (4PA), respectively.

2.2.2. THz Generation in Lithium Niobate

THz generation from LN was demonstrated as early as 1971.[31] The efficiency was extremely low due to a lack of phase matching. Introduction of the TPFP technique[43] enabled more efficient THz pulse generation from this material (see empty symbols in **Figure 5**) and an increase of the THz pulse energy by several orders of magnitude.[54,55] The potential of the technique for high-energy THz pulse generation was demonstrated in subsequent experiments, where 10 µJ[56] and 50 µJ[57] pulse energies were reported with efficiencies of about 5×10^{-4}. Peak electric-field strengths of up to 4 MV cm^{-1} were reported.[58–60] In these experiments, short pump pulses were used, with pulse durations of about 100 fs or less.

With this progress, however, some limitations became also apparent. As mentioned above, a straightforward way to increase the THz pulse energy in TPFP is to increase the spot size and the pump energy. Conventional pulse-front-tilting

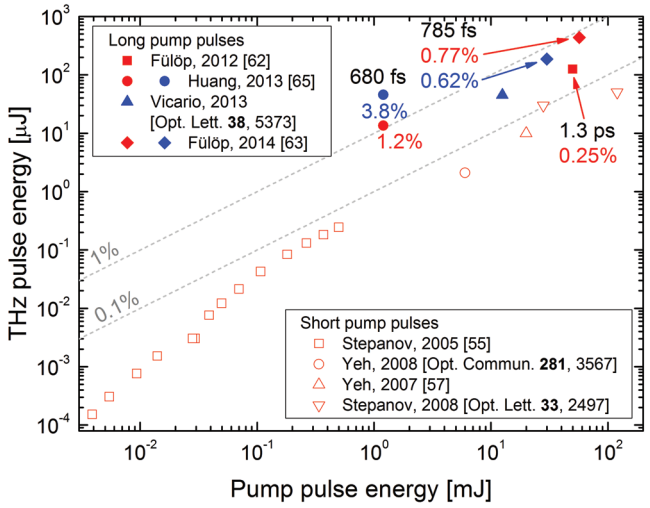

Figure 5. Measured scaling of the THz pulse energy with the pump pulse energy in LN using TPFP with short (about 100 fs) and long (0.5–1.5 ps) pump pulses. Red (blue) symbols: room (cryogenic) crystal temperature. The dashed gray lines indicate the 0.1% and the 1% levels of pump-to-THz energy conversion efficiency.

setups consist of a diffraction grating, which creates the PFT, and imaging optics (usually a lens or a telescope), which restores the short pulse duration and eliminates the spatial dispersion of the spectral components inside the nonlinear crystal (**Figure 6**). Imaging errors can lead to spatial distortions of the THz beam[37] and a reduced THz yield in case of large pump beams.[61] Optimization of the imaging system can reduce such distortions,[37,61] which played a role in increasing the THz pulse energy further,[62,63] but the useful beam size still remained limited to about 1 cm.

A further significant increase in efficiency and THz pulse energy became possible by optimizing the Fourier-limited pump pulse duration τ_0.[37,64] As mentioned above (Section 2.1), PFT is linked to angular dispersion and group-velocity dispersion. As a large PFT angle of about 63° is needed for phase matching in LN, the corresponding group-velocity dispersion dominates over that from material dispersion and causes a variation of the pump pulse duration within the nonlinear medium.[64] **Figure 7**a shows this variation for different values of τ_0 and 0.8 µm pump wavelength. The pulse duration changes rapidly for a pulse with short τ_0, but it changes much less for long τ_0 (Figure 7a). OR is most efficient in the crystal region where the pump pulse duration is the shortest (closest to its Fourier limit) and, consequently, the pump intensity is the highest. The position of

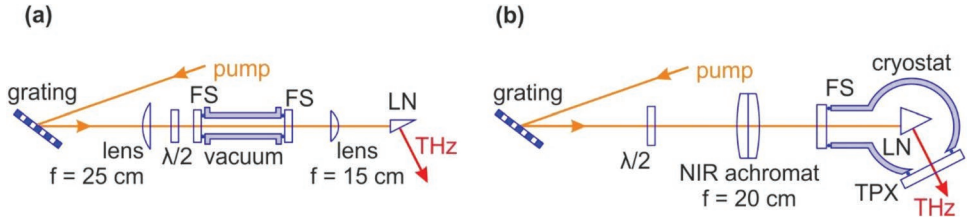

Figure 6. Typical setups for high-energy THz pulse generation by TPFP in LN using a) a telescope and b) lens for PFT. The focal regions of the lenses are located in vacuum to avoid nonlinear effects in air. For cryogenic cooling, the LN crystal is also held in vacuum.

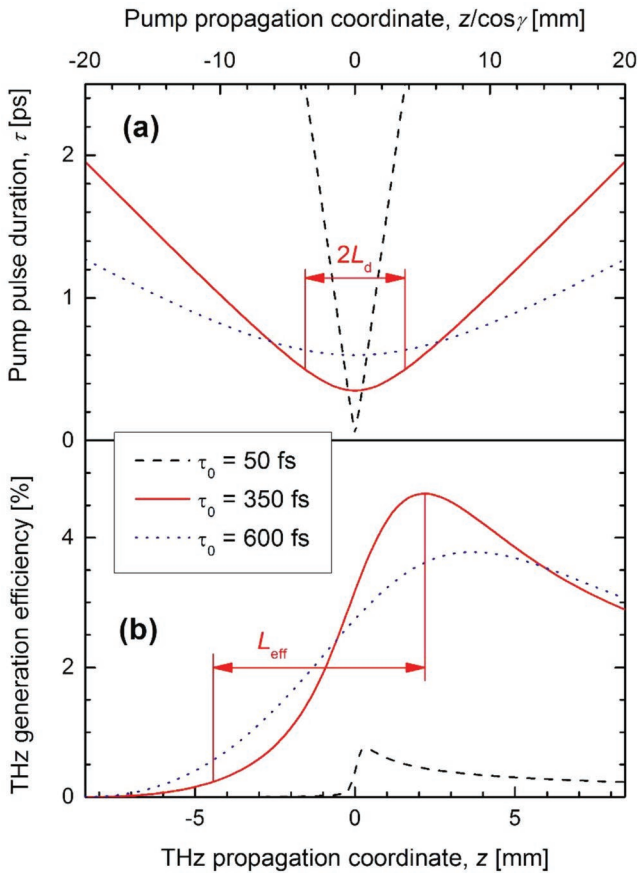

Figure 7. a) Calculated variation of the pump pulse duration inside the LN crystal for three different values of the Fourier-limited pulse duration and 0.8 µm pump wavelength. b) The corresponding accumulated THz generation efficiencies. Reproduced with permission.[37] Copyright 2010, The Optical Society of America.

this region within the crystal can be adjusted by the prechirp of the pulse. The length of this region is characterized by the dispersion length $2L_d$, where the pump pulse duration does not exceed $\sqrt{2}\tau_0$. The THz field can build up over the corresponding effective interaction length L_{eff} (Figure 7b). Outside this region, absorption dominates, and the THz pulse gets attenuated. For short pulses, the interaction length is very short and the maximum efficiency remains very small. Longer pulses are, therefore, more advantageous. On the other hand, the maximum efficiency decreases for very long pulses, resulting in an optimum pump pulse duration with highest efficiency.

Figure 8a shows the calculated dependence of the maximum efficiency as function of the Fourier-limited pump pulse duration for LN pumped at 1 µm wavelength. The highest efficiency is predicted for longer pulses of about 500 fs Fourier-limited pulse duration, while the conventionally used ≈100 fs pulses give 6 × smaller efficiency. The advantage of longer pump pulse duration was first demonstrated in a pilot experiment with 1.3 ps pump pulses, resulting in the generation of 125 µJ THz pulses with 0.25% efficiency,[62] 2.5 × higher both in energy and efficiency than reported previously with shorter pulses (Refs. [57] and, [58] respectively). Later, by using a nearly optimal pulse duration of 780 fs, an efficiency as high as 0.77% was demonstrated, and THz pulses with the so far highest energy from LN of more than 0.4 mJ were generated.[63] Further improvement can be achieved with cooling of the crystal to cryogenic temperatures (Figure 8a), thereby reducing its absorption in the THz range. With a cooled source, as high as 3.8% conversion efficiency was reported at a small pump energy of 1.2 mJ by using close-to-optimal pump pulse duration.[65] Such a high efficiency could not yet be demonstrated at higher energies. It can be expected that in the near future THz pulses with multi-mJ energy will become available from cooled LN sources based on TPFP.

Utilizing longer pump pulses implies a shift of the generated THz spectrum toward lower frequencies (Figure 8b). While for τ_0 = 100 fs, the peak of the THz spectrum is at 1.1 THz, for 500 fs it is at about 0.4 THz. For spectroscopy or resonant control of matter, the shift of the spectrum to lower frequencies is often disadvantageous. However, for manipulation and acceleration of charged particles, this frequency range is optimal (see also Section 5). Pulses suitable for the acceleration of proton[17,63] or electron[23] bunches have already been demonstrated experimentally.

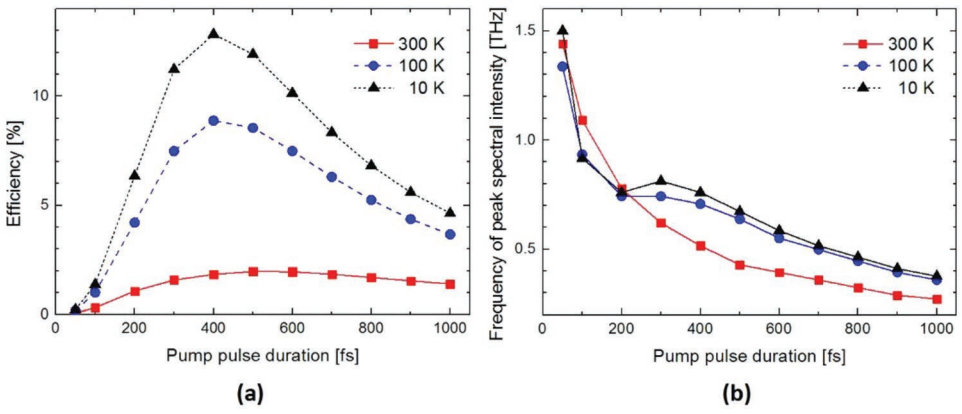

Figure 8. a) Calculated THz generation efficiency and b) the frequency of the maximum spectral intensity as functions of the Fourier-limited pump pulse duration in LN pumped at 1 µm wavelength. Results are shown for three different crystal temperatures. Reproduced with permission.[64] Copyright 2011, The Optical Society of America.

Table 1. Limiting effects and possible solutions for THz generation by the TPFP technique.

Limiting effect	Possible solution
Variation of pump pulse duration inside the nonlinear medium due to pulse-front tilt	• Longer Fourier-limited pump pulses • Materials requiring smaller pulse-front tilt
Absorption at THz frequencies: • Linear absorption determined by the complex dielectric function • Free-carrier absorption caused by multiphoton absorption at the pump wavelength	• Cool the crystal to reduce linear absorption • Use longer pump wavelength to suppress low-order multiphoton absorption
Nonuniform interaction length in a prism-shaped nonlinear crystal	• Materials requiring smaller pulse-front tilt • Nonlinear echelon slab (NLES, see Section 2.2.4)
Walk-off between pump and THz due to the noncollinear geometry	• Large pump beam and energy • Materials requiring smaller pulse-front tilt
Imaging errors for large pump spot sizes	• Optimized imaging system • Hybrid system (imaging + contact grating) • Contact grating (imaging-free) • Nonlinear echelon slab without imaging

2.2.3. Limitations and Their Solutions

Table 1 summarizes various effects limiting the efficiency of THz generation and the achievable field strength in TPFP schemes. Possible solutions for reducing or eliminating such limiting effects are also given in Table 1. In case of LN, the use of longer Fourier-limited pump pulses and cryogenic cooling of the crystal were discussed above. Walk-off between pump and THz imposes a geometric limit for the interaction length, which depends on the pump beam size. Therefore, large interaction lengths, enabled by long pump pulses and the reduced absorption coefficient at low temperature, can only be utilized with a sufficiently large pump beam size and pump energy. It shall be noted that semiconductor nonlinear materials require advantageously smaller PFT angles (see Section 2.3).

Sum- and difference-frequency mixing of the pump and an intense THz field can lead to a significant spectral broadening of the pump. For short crystals, this effect can favorably result in increased THz bandwidth and, consequently, a higher peak electric field.[41] For longer crystals, typically used in high-energy THz sources, the consequence of the THz-induced spectral broadening of the pump can be a significantly reduced efficiency,[42] as shown in **Figure 9**a. A broadening of the pump spectrum causes the decrease of the (Fourier-limited) pump pulse duration, which leads to reduced dispersion and effective interaction lengths,[66] as shown in Figure 9b for the dispersion length L_d (see also Figure 7). It can also lead to intensity-dependent distortions of the THz beam.[66]

A compact TPFP THz source was proposed by using a contact grating (CG).[61] This approach offers a new perspective for scalable and efficient THz pulse generation. Because no imaging optics are needed for PFT, it is free of the associated distortions. The implementation is challenging in the case of LN, owing to its large optical refractive index and the required large PFT angle. To improve the efficiency of coupling, the pump light into the nonlinear medium, a refractive-index-matching liquid (**Figure 10**a),[67] or a Ta_2O_5–Al_2O_3 multilayer

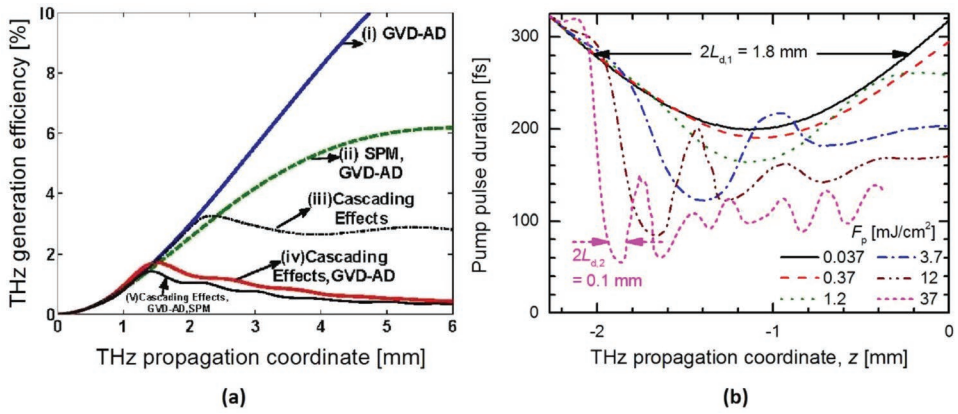

Figure 9. a) Calculated THz generation efficiency as a function of the THz propagation distance in LN for 500 fs pulses. Limitations of the conversion efficiency caused by various nonlinear effects are compared. AD: angular dispersion, GVD: group velocity dispersion, SPM: self-phase modulation. Reproduced with permission.[42] Copyright 2014, The Optical Society of America. b) Calculated pump pulse duration as function of the THz propagation coordinate in LN for 200 fs pulses at various pump fluence levels. Reproduced under the terms of the Creative Commons Attribution 3.0 License.[66] Copyright 2015, IOP Publishing.

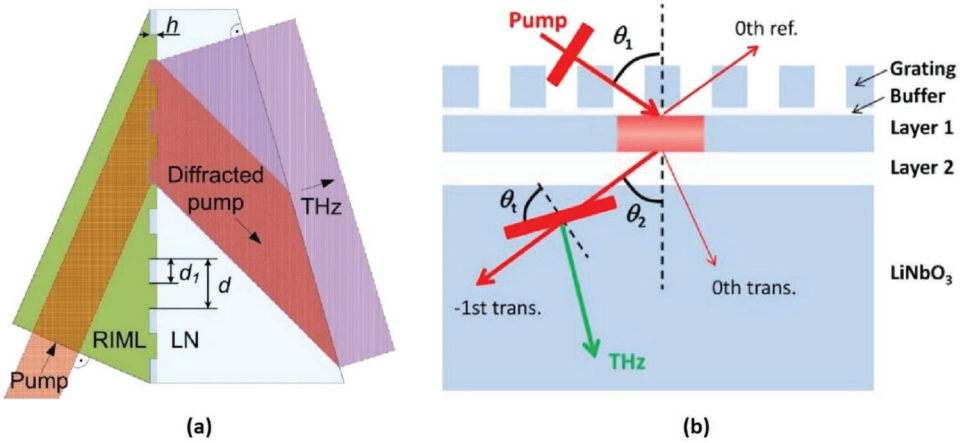

Figure 10. Contact-grating setups for TPFP in LN using a) a refractive-index-matching liquid (RIML), and b) a multilayer structure satisfying conditions for a Fabry–Perot resonator. The thick red lines indicate the pump pulse front. a) Adapted with permission.[67] Copyright 2012, Springer Nature. b) Reproduced with permission.[68] Copyright 2014, The Optical Society of America.

formed on the LN substrate (Figure 10b)[68] was proposed. In the latter case, the grating was fabricated on the outermost layer. The multilayer was designed such to satisfy conditions for a Fabry–Perot resonator for the diffracted light. With this device, a THz output of 0.41 µJ was demonstrated using 2.7 mJ of near-infrared pump light.

Recently, the combination of a conventional TPFP setup using imaging and a CG was proposed,[69] in which imaging distortions can be significantly reduced and less stringent requirements on the grating profile have to be fulfilled. Even though in such hybrid setups, a prism-shaped LN crystal needs to be used with ≈30° wedge angle, this angle is sufficiently small to significantly reduce transverse nonuniformity across beams as large as 1 cm. It is expected that LN hybrid CG schemes are scalable to high THz pulse energies beyond 1 mJ.

2.2.4. Novel Scalable Concepts

In the conventional source geometry, the prism-shaped LN crystal has a large wedge angle equal to the PFT (63°). In the hybrid CG scheme, the wedge angle still amounts to about 30°. Consequently, the pump propagation length becomes nonuniform across the beam, leading to a spatially varying interaction length for THz generation. This effect can cause lateral waveform nonuniformity (**Figure 11**b), which is especially problematic in extremely high-energy THz sources, where a pump beam diameter larger than 1 cm is needed. The THz beam quality and, consequently, focusability can suffer from such effects, thereby seriously limiting the achievable field strength.

A plane-parallel contact-grating THz source with uniform interaction length could be successfully demonstrated in ZnTe[45] (see also Section 2.3), but the realization of a practical (hybrid) contact-grating source in LN so far turned out to be very challenging. Recently, a modified hybrid approach was proposed to provide uniform interaction length across large pump and THz beams.[70] A proof-of-principle experimental demonstration has also been carried out.[71] In this setup, the nonlinear medium is a plane-parallel LN slab with an echelon structure on its input surface (Figure 11a). Inside the LN slab, a segmented tilted pulse front is formed with an average tilt angle as required by phase matching. It has also been shown that the imaging can be omitted, resulting in even more robust and compact setups.[71,72] We note that a reflective echelon has

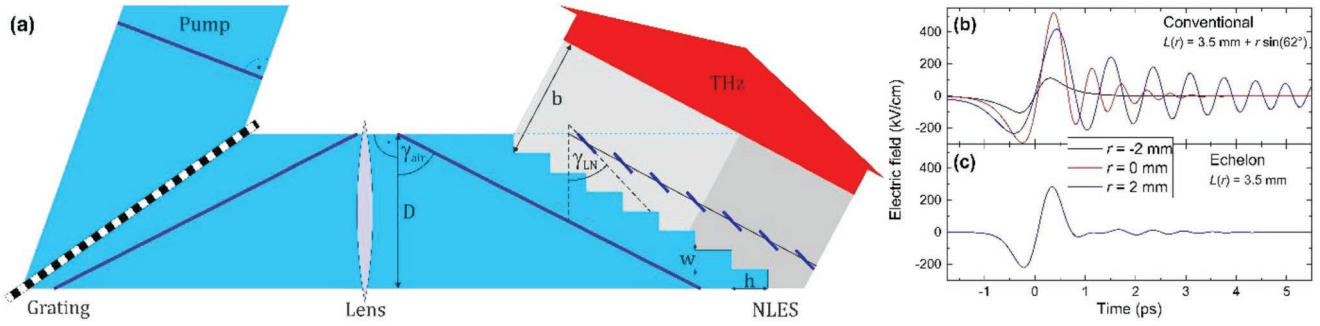

Figure 11. a) Scheme of TPFP THz source based on an LN nonlinear echelon slab. Calculated THz-pulse waveforms at different positions across the THz beam for an b) LN prism and c) a plane-parallel LN slab. The lateral position in the input pump beam is labeled by *r*, where $r = 0$ corresponds to the beam center. $L(r)$ is the corresponding material length along the THz propagation direction. Reproduced with permission.[71] Copyright 2019, The Optical Society of America.

been used earlier for tilting the average pump pulse front for efficient THz generation in LN, but this approach still requires the use of a prism-shaped LN crystal with the same wedge angle as in the conventional setup.[73]

A comparison of the output THz waveforms in a conventional prism-shaped LN crystal and those in a plane-parallel LN slab with an echelon clearly illustrates the importance of a uniform interaction length across the pump and THz beams. Whereas the waveform strongly varies across the beam in the former case (Figure 11b), it can be almost perfectly uniform in the latter case (Figure 11c). This uniformity is essential for a straightforward scalability to extremely high THz pulse energies by simply increasing the pump spot size and energy, as well as to produce the highest possible THz peak field strengths by the excellent focusability. This new technology opens up the way to the construction of efficient sources of extremely high-energy THz pulses with excellent focusability for extremely high field strengths in the 5–50 MV cm^{-1} range.

Finally, we mention that significant recent work has been devoted to the efficient generation of narrowband multicycle THz pulses. By using periodically poled LN, THz pulses with 0.361 THz frequency, less than 1% relative bandwidth, and as high as 0.6 mJ energy have been reported.[74] Applications involving selective excitation of states for spectroscopy and control of materials, as well as efficient THz-driven particle accelerators can benefit from this exciting development.

2.3. Semiconductor Nonlinear Materials

Semiconductors are among the most frequently used nonlinear optical materials for OR, DFG, and optical parametric amplification (OPA). Semiconductors are also applied as detectors in electric-field waveform measurement of broadband THz pulses, using (unbiased) photoconductive antennas or electro-optic sampling.[12]

THz pulse energies on the order of 1 µJ were demonstrated both with OR[44,75] and OPA.[76] Multicycle THz pulses at multi-10 THz frequencies were generated with energies up to 19 µJ by DFG.[77] Recent developments indicate that OR will expectedly be scalable to substantially higher, mJ-level energies.[45,46] For this reason, OR in semiconductors is discussed here in more detail.

2.3.1. Basic Properties

Important properties of semiconductors relevant for THz generation by OR were compiled in refs. [4,34–37,52]. In brief, the main features are:

- Semiconductors possess nonlinear coefficients smaller than that of LN and organic crystals, typically falling into the range of 25–80 pm V^{-1}.
- The linear absorption coefficient of many semiconductors in the THz range is smaller than that of LN or organic crystals, which can partially compensate for their smaller nonlinearity. Semiconductors with higher phonon frequency can enable the generation of higher THz frequencies, such as GaP up to about 7 THz.[35,78]
- Many semiconductors (e.g., CdTe, GaAs, GaP, ZnTe) are optically isotropic. In some cases, collinear phase matching for OR is fulfilled at a specific pump wavelength. Notable examples are ZnTe pumped around 0.8 µm, GaP pumped around 1 µm, or GaAs pumped around 1.5 µm, where commercially available Ti:sapphire, Yb-doped, or Er-doped pump lasers can be used. At longer pump wavelengths, TPFP has to be used for phase matching.[37,39] Phase matching utilizing birefringence can be accomplished in GaSe above the Reststrahlen band.
- At common pump wavelengths used for collinear phase matching, semiconductors exhibit two-photon absorption (2PA), which leads to a serious limitation of the achievable THz generation efficiency. A solution can be to use longer pump wavelengths, where only higher-order multiphoton absorption (MPA) is effective. The issue of MPA is discussed below in more detail.

2.3.2. Free-Carrier Absorption

The bandgap of the most relevant semiconductors is much smaller than that of LN (3.8 eV). For example, in ZnTe it is 2.26 eV. At the typical pump wavelength of 0.8 µm (1.55 eV photon energy), this feature results in strong 2PA already at moderately high pump intensities. The consequence is a transiently increased free-carrier concentration. The density of free carriers n_{fc}, generated by the pump pulse, can be calculated as[37,39]

$$n_{fc} = \frac{I\tau}{hc/\lambda_0}\left(\alpha + \frac{1}{2}\beta_2 I + \frac{1}{3}\beta_3 I^2 + \frac{1}{4}\beta_4 I^3 + \cdots\right) \quad (8)$$

Here τ is the pump pulse duration, I is the time-averaged pump intensity, $\lambda_0 = 2\pi c/\omega_0$ is the central wavelength of the pump, α is the linear absorption coefficient, β_2, β_3, and β_3 are the two-, three-, and four-photon absorption coefficients, respectively. The increased free-carrier concentration results in increased absorption at THz frequencies, thereby limiting the THz

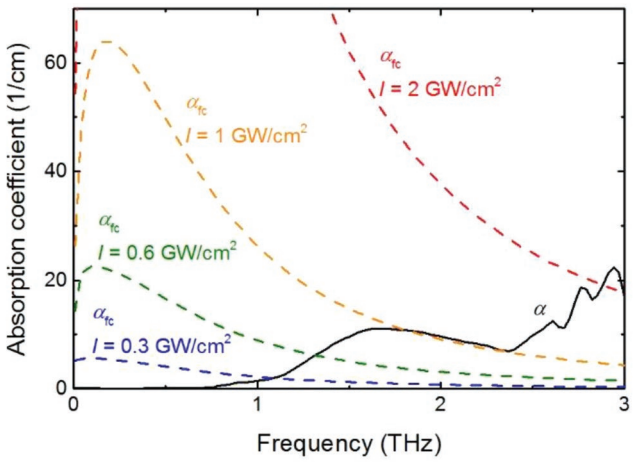

Figure 12. Linear absorption coefficient α originating from the imaginary part of the complex dielectric constant (black solid curve) and FCA coefficients αfc in ZnTe, at various pump intensity levels (dashed curves), as functions of the THz frequency. The FCA coefficients were calculated with β_2 = 4.2 cm GW^{-1}, 0.8 µm pump wavelength, and 100 fs pulse duration.

generation efficiency. The free-carrier absorption (FCA) coefficient, $\alpha_{fc}(\Omega)$, can be calculated with the Drude-model[37,79] as

$$\alpha_{fc}(\Omega) = \frac{2\Omega}{c}\,\mathrm{Im}\sqrt{\varepsilon_\infty \cdot \left(1 - \frac{\omega_p^2}{\Omega^2 + i\Omega/\tau_{sc}}\right)} \quad (9)$$

Here, ε_∞ is the high-frequency dielectric constant, τ_{sc} is the electron scattering time, $\omega_p^2 = e^2 n_{fc}/(\varepsilon_0 \varepsilon_\infty m_{eff})$ is the plasma frequency, and e and m_{eff} are the electron charge and effective mass, respectively. For example, in ZnTe pumped at 0.8 µm, FCA due to 2PA becomes comparable to the linear absorption at 1 THz already below 1 GW cm^{-2} pump intensity (**Figure 12**).

The limitation imposed by FCA on the useful pump intensity and on the achievable THz generation efficiency is a serious restriction for high-energy THz pulse generation. To avoid such saturation effects, the use of large-area emitter crystals was proposed.[80] By using a Ti:sapphire laser source with 30 fs pulse duration and a 75 mm diameter, 0.5 mm thick ZnTe crystal wafer, the generation of 1.5 µJ single-cycle THz pulses with a spectral range extending to 3 THz was demonstrated.[75] The energy conversion efficiency was 3.1×10^{-5}, strongly limited by FCA caused by 2PA.

For Yb-doped laser-technology, GaP, an indirect bandgap semiconductor, can be a more suitable choice for THz generation. It is collinearly phase-matched around the 1 µm wavelength.[81] At such a pump wavelength, only indirect 2PA and direct 3PA are possible, which have smaller absorption coefficients than that of direct 2PA.[39] This property and the smaller phonon absorption in the low-frequency THz range can compensate for the relatively small nonlinear coefficient of GaP. Nevertheless, the demonstrated efficiencies remained very small in comparison to LN.[39] Consequently, semiconductors were long considered to be unsuitable for high-energy THz pulse generation.

2.3.3. Novel Concepts for Infrared Pumping

More recently, however, semiconductors were reconsidered for high-energy THz pulse generation, when prospects of pumping at longer infrared wavelengths were investigated.[37] This approach enables the elimination of low-order MPA at the pump wavelength and the associated FCA at THz frequencies. For example, in the case of ZnTe, the cut-off wavelength for 2PA (3PA, etc.) is at 1.10 µm (1.65 µm, etc.). At longer pump wavelengths, only 3PA (4PA, etc.) and higher-order MPA are effective, thereby enabling a higher pump intensity to be efficiently used for THz generation. We note that the saturation of FCA, caused by 2PA, was recently observed in ZnTe at high pump fluences.[82] This finding indicates that saturation of MPA may contribute to the further improvement of the THz yield in semiconductor THz sources.

At longer pump wavelengths, where the optical group velocity is larger than the THz phase velocity, TPFP has to be used for phase matching in most cases. An important advantage of semiconductors over LN is the much smaller PFT angle required for phase matching. It is typically below 30°, in contrast to LN, where it is about 63° (**Figure 13**). We note that in the case of birefringent materials, such as GaSe, phase matching by angle tuning is possible for THz generation at higher frequencies above the transverse-optical phonon resonance (see Section 2.3.4).

THz pulses with 0.6 µJ energy were recently generated with 5×10^{-4} efficiency from a GaAs TPFP source pumped at 1.8 µm, above the cut-off wavelength for 2PA.[44] This efficiency is more than one order-of-magnitude higher than that achieved previously with 0.8 µm pumped ZnTe.[75] The reason is the elimination of 2PA by the sufficiently long pump wavelength in case of GaAs. More recently, a comparative study in ZnTe demonstrated a 3.5-fold increase of the THz generation efficiency when pumped at 1.7 µm, rather than at 1.45 µm.[46] The pump wavelengths of 1.45 and 1.7 µm are sufficiently long to suppress 2PA and 3PA, respectively, and the 3PA coefficient has an expected minimum around 1.45 µm. Up to 14 µJ THz energy with the spectral peak around 0.7 THz was demonstrated with an extremely high efficiency of up to 0.7% in a ZnTe prism pumped at 1.7 µm, above the cut-off for 3PA.[46] Such a high efficiency is comparable to that achieved with LN at high pulse energies[63] and clearly shows the potential of semiconductors for high-energy THz pulse generation.

A further increase in THz energy and field strength can be expected from increasing the source size and the pump energy. A promising possibility is offered by utilizing the CG technique

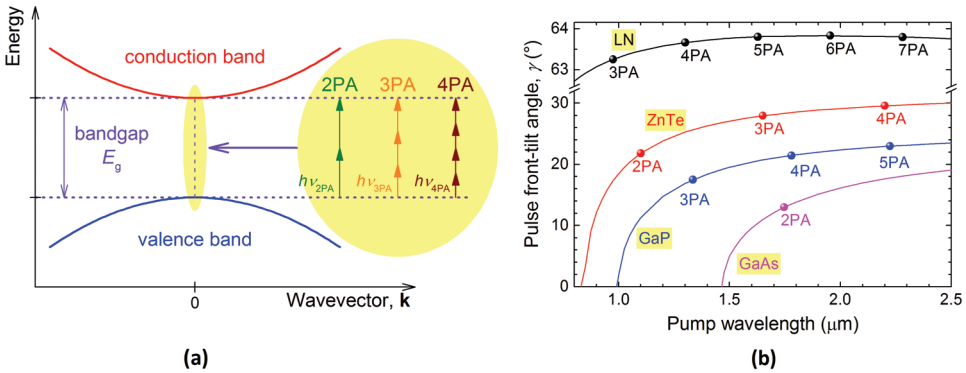

Figure 13. a) Schematic electronic band structure of a direct-bandgap semiconductor with the schemes of MPA of various orders. b) PFT angle versus pump wavelength for phase matching at 1 THz in LN and selected semiconductors. The symbols indicate the cut-off wavelengths for MPA of various orders. In case of GaP, the direct bandgap is considered. Adapted with permission.[46] Copyright 2016, The Optical Society of America.

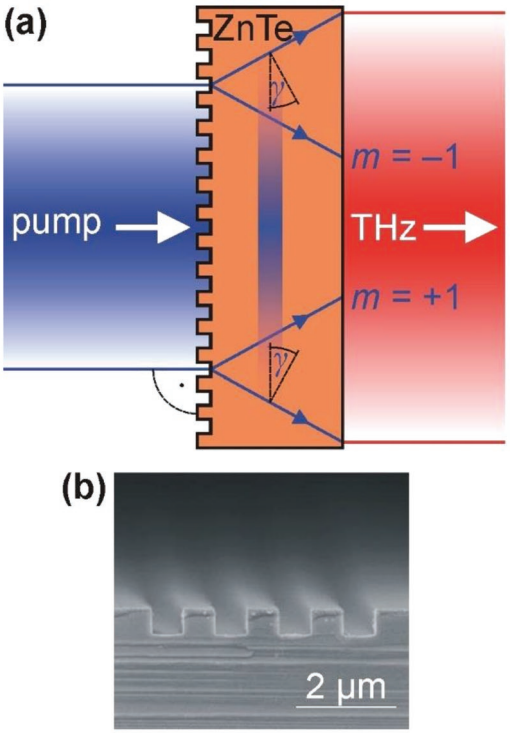

Figure 14. a) Scheme of a semiconductor CG THz source with collinear geometry. b) Scanning electron microscope image of a cleaved CG test sample showing the binary line profile required for high diffraction efficiency. Reproduced with permission.[45] Copyright 2016, The Optical Society of America.

(**Figure 14**).[45,61,83] Owing to the small PFT angles required for phase matching (Figure 13b), semiconductors are particularly suitable for this compact and monolithic technology. The first demonstration of this technique with a ZnTe CG pumped above the cut-off for 3PA[45] resulted in 3% THz generation efficiency, two orders of magnitude higher than the previously reported highest value for ZnTe.[75] The THz pulse energy was 3.9 μJ. The efficiency can be increased further by increasing the crystal length. These results support the expectation that THz pulses with 1 mJ energy can be generated with less than 200 mJ pump energy from a (possibly segmented) CG source of about 5 cm diameter. This new THz source, in combination with efficient infrared pump sources in the 1.7 to 2.5 μm wavelength range based, e.g., on Ho- or Cr-based laser technology,[84] opens up new perspectives for THz high-field applications.[85] For example, it can become a key technology for compact THz-driven particle accelerators.[17,23]

Certain applications, such as the resonant excitation of materials in (nonlinear) THz spectroscopy or THz-driven electron acceleration in waveguide, resonator, and dielectric grating structures require multicycle THz pulses. Whereas laser-driven THz sources typically deliver single-cycle or nearly-single-cycle waveforms, the generation of multicycle THz waveforms can be difficult. In the case of phase-matched OR, the THz waveform is determined by the intensity shape of the pump pulse.[29] Thus, one of the main technical challenges is to create suitably shaped intensity-modulated pump pulses, ideally with a versatile

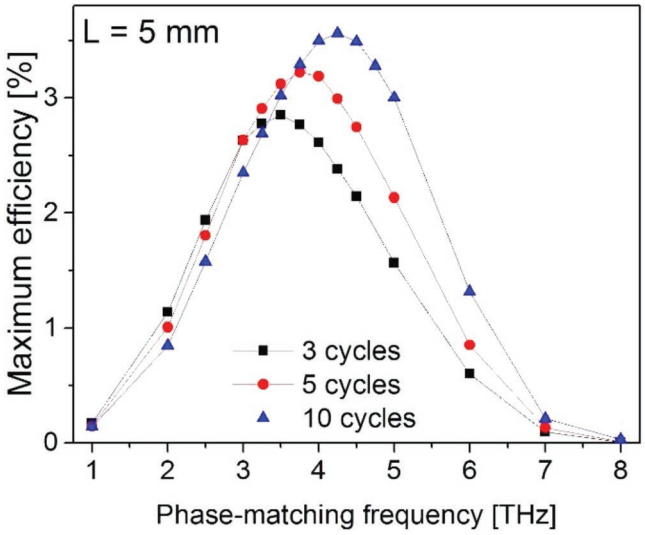

Figure 15. Calculated maximum achievable THz generation efficiency for the respective optimal pump intensities as function of the THz frequency, for three-, five-, and ten-cycle THz pulse generation. The GaP crystal length was 5 mm in all cases. Reproduced with permission.[78] Copyright 2018, IOP Publishing.

shaping capability. Recently, Tóth et al. have proposed an efficient method to generate high-energy infrared pump pulses with a constant intensity-modulation period suitable for multicycle THz pulse generation.[86] This source of flexibly shapeable pump pulses is ideally suited to drive a multicycle THz source based on GaP, ZnTe, or GaAs nonlinear materials.[78] GaP can offer a relatively broad tuning range up to about 7 THz (**Figure 15**). A high efficiency of >3% is predicted, and the pulse energy can easily be increased by using a large nonlinear-optical crystal.

2.3.4. Generation of Higher THz Frequencies

Contrary to the low-frequency part of the THz spectrum, the potential of semiconductors was recognized earlier for high-field THz pulse generation in the high-frequency part of the THz spectrum. Generation of pulses tunable over the entire high-frequency THz (mid-infrared) range from 15 to 75 THz (between 20 and 4 μm wavelengths) was demonstrated by DFG in GaSe.[87] The near-infrared signal and idler pulses from an optical parametric generator were used for DFG. Phase matching was accomplished by angle tuning, utilizing the birefringence of GaSe. Carrier-envelope-phase-stable mid-infrared pulses were generated in a related scheme in GaSe, based on type-II DFG between the signal pulses from two OPAs, derived from the same white-light seed.[77] Multi-cycle pulses tunable from 10 to 70 THz and focused electric field strengths up to 100 MV cm^{-1} were demonstrated with this technique (**Figure 16**). Using type-I OPA in GaSe, phase matching with larger bandwidth could be achieved, and single-cycle pulses, centered at 25 THz, with up to 10 MV cm^{-1} field strength were generated.[76] The high THz frequency was essential in reaching such high field strengths, because the conversion efficiency (Equation (4)), the diffraction-limited focal spot size, and the pulse duration scale favorably with increasing frequency.

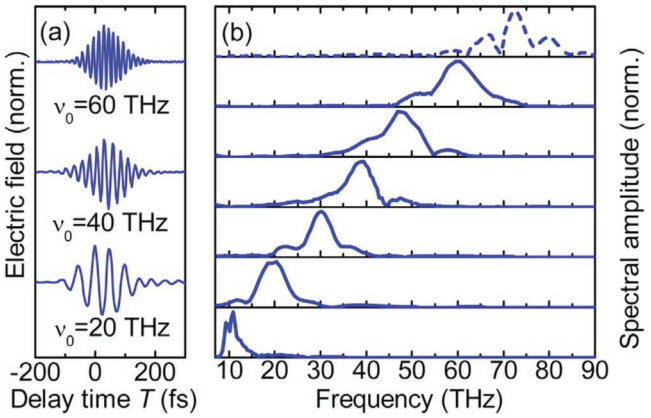

Figure 16. a) Waveforms and b) amplitude spectra of high-frequency THz pulses generated by DFG in GaSe of 140 µm length (solid lines) and $AgGaS_2$ of 800 µm length (dashed line). Reproduced with permission.[77] Copyright 2008, The Optical Society of America.

2.4. Organic Nonlinear Materials

Recently, organic crystals have gained increasing attention for the generation of intense THz pulses by OR. Organic THz emitters such as DAST,[88–92] DSTMS,[92,93] OH1,[92,94] HMQ-TMS[38] can provide high optical-to-THz conversion efficiencies at room temperature and octave-spanning, or even multi-octave THz spectra. They have the largest nonlinear coefficients among materials used for OR. In case of DAST, e.g., it is $d_{\text{eff}} = 615$ pm V^{-1}.[36,95] Organic crystals are best suited for accessing intervals, separated by phonon resonances, in the mid-frequency (1–20 THz) part of the THz range.[90,96]

For phase-matched OR, organic crystals typically require infrared pump wavelengths in the 1.2–1.6 µm spectral range (**Figure 17**), where a collinear geometry can be used for THz generation. Phase matching at the 0.8 µm wavelength of Ti:sapphire lasers is usually possible only at low frequencies below 1 THz. Organic crystals typically have several phonon absorption bands in the mid-frequency THz spectral range. The associated anomalous dispersion of the THz refractive index can enable simultaneous phase matching in different THz spectral bands, which are separated by absorption bands. The complicated phase-matching behavior is illustrated in Figure 17a, showing the coherence length for OR in HMQ-TMS.[96] Consequently, the spectral intensity (Figure 17b) and phase structure of the generated THz pulses becomes complex, often leading to multicycle waveforms. Variation of the pump wavelength was utilized for controlling the spectral coverage of the generated THz pulses (Figure 17b).[96]

Owing to the collinear phase matching geometry, the generated THz radiation is naturally collimated, enabling a good focusability of the beam for achieving high field strengths. High-power single-cycle THz pulses at a central frequency of 2.1 THz with 1 MV cm^{-1} electric and 0.3 T magnetic field strengths in focus were demonstrated by OR in DAST pumped with 1 mJ signal pulses of an infrared OPA.[91] The pump-to-THz conversion efficiency was as high as 2%.

White-light-seeded OPAs are unfavorable as pump source for THz generation because of their low optical-to-optical conversion efficiency, the often irregular beam profile containing hot spots, and the large shot-to-shot energy fluctuation. These features limit the maximum usable pump fluence and can result in unstable THz emission.[92,97] As an alternative, Cr:forsterite lasers, operating around 1.25 µm wavelength, enable efficient direct pumping of organic crystals. Larger than 10 MV cm^{-1} electric and 3 T magnetic field strengths were achieved with up to 3% efficiency by using such a laser to pump different organic crystals.[92]

Possible limitations of the available crystal size can be overcome by using partitioned crystals.[89,97] High-field THz transients were reported with as high as 0.9 mJ energy, produced in a 400 mm^2 partitioned DSTMS crystal by OR of 30 mJ laser pulses, delivered by a Cr:forsterite laser.[93] The frequency range covered was between 0.1 and 5 THz. The peak THz electric and magnetic field was 42 MV cm^{-1} and 14 T, respectively. The conversion efficiency was as high as 3%. By optimizing the THz wavefront curvature for diffraction-limited focusing as high as 80 MV cm^{-1} (27 T) focused peak electric (magnetic) field has been reported from DSTMS for the moderate THz pulse energy of 109 µJ in the 0.1–5 THz spectral range.[98] These results clearly demonstrate the potential of organic-crystal THz sources for strong-field science.

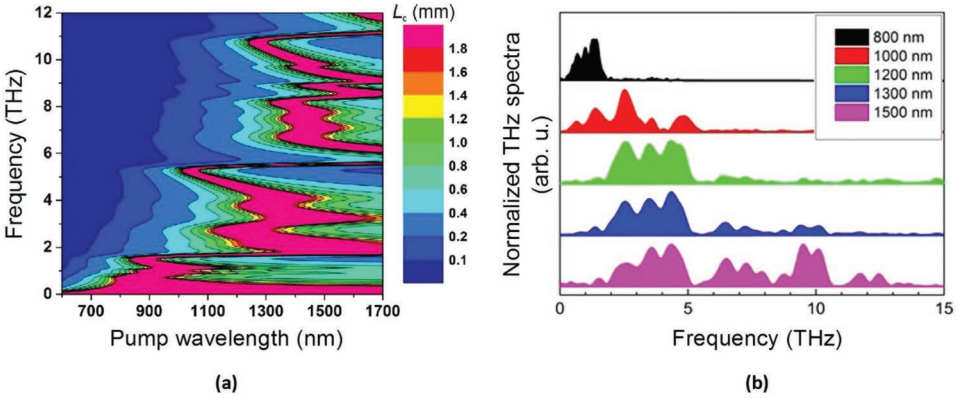

Figure 17. a) Coherence length $L_c = \pi/\Delta k$ for HMQ-TMS as a function of optical pump wavelength and THz frequency. b) Experimentally recorded THz spectra for various pump wavelengths. Reproduced under the terms of the Creative Commons Attribution 4.0 License.[96] Copyright 2015, Springer Nature.

3. Solid-State Photocurrent THz Emitters

3.1. Semiconductor Photoconductive Antennas

In the previous sections, the generation of the THz polarization or, equivalently, THz charge current arose from OR because the incident photon energy was below the electronic band gap of the insulator or semiconductor used. For above-band-gap excitation, the response is usually dominated by the generation of charge carriers and a photocurrent with a temporally step-like onset. However, the photocurrent decays on a time scale that is typically substantially longer than the sub-100 fs duration of the driving optical pulse. Consequently, its bandwidth is smaller than that of the induced nonlinear polarization in case of OR,[99] which approximately lasts as long as the driving optical pulse is present in the material.

3.1.1. Basic Concept

Currently, the most efficient photocurrent emitters for strong-field applications based on semiconductors are large-area photoconductive antennas.[12,100–102] As schematically shown in **Figure 18**a, in these devices, an external bias voltage breaks the in-plane inversion symmetry and accelerates the optically generated carriers. The resulting macroscopic in-plane current leads to the emission of THz radiation into the far-field. Note that in this process, the energy of the THz pulse derives from the bias field rather than from the driving laser pulse.

Large-area photoconductive emitters were demonstrated as early as 1993.[100,101] Using GaAs, a bias field of 10.7 kV cm^{-1} over an antenna gap of 3.5 cm and optical pulses with 120 fs duration and 770 nm center wavelength, THz pulses with an energy of up to 0.8 µJ and a field of ≈150 kV cm^{-1} have been reported.[100]

3.1.2. Recent Developments

The bias field of large-area photoconductive antennas leads to a large thermal load due to Ohmic losses of the photocurrent within the material (Joule heating), dielectric breakdown, and material degradation. To mitigate these issues, semiconductors with large electronic bandgap, high thermal conductivity, and high carrier mobility should be used.[12,102] Along these lines, ZnSe[102] and, in particular, 6H-SiC[103] were recently shown to be promising materials. In addition, to reduce the bias voltage while maintaining a bias field on the order of 10 kV cm^{-1} over a length of ≈1 cm, multiple electrode pairs with smaller cathode–anode distance rather than one pair are used (see Figure 18b).[102,104] To prevent destructive superposition of THz waves from regions with opposite bias, every other gap is either blocked by a shadow mask[104] or its emission is phase-shifted by 180° using a phase mask.[102]

Using this strategy and a ZnSe interdigitated 12.2 cm^2 large-area photoconductive antenna with a phase mask and 2.5 mJ, 400 nm laser pulses, THz pulses with an energy of 8.3 µJ and peak electric field of 331 kV cm^{-1} in the focus were demonstrated.[102] Figure 18c displays an example waveform from a ZnSe emitter with shadow mask, while Figure 18d shows that the spectrum covers the range from < 0.05 to 1 THz.

We finally note that large-area photoconductive emitters have small-area counterparts with lateral dimensions on the order of 100 µm. They are driven by laser oscillators and deliver accordingly smaller THz fields, which are routinely applied in linear spectroscopy.[105] Recently, the incorporation of plasmonic nanostructures into the electrodes was reported to lead to an enhanced generation of photocarriers close to the metal contacts, resulting in a 50 times higher emitted THz power output as compared to standard electrodes.[106] Transferring this approach to photoconductive emitters with ≈1 cm lateral dimensions is highly promising, but not straightforward with current nanostructuring technology.

3.2. Spintronic THz Emitters

Semiconductors and insulators are currently the most frequently used base materials of solid-sate THz sources, both in terms of OR and photocurrents. Since most semiconductors used are polar (such as ZnTe,[75] GaP,[81] GaSe,[77] GaAs,[44] or organic materials[91]) and strongly attenuate THz radiation around optical phonon resonances, emission is reduced in the

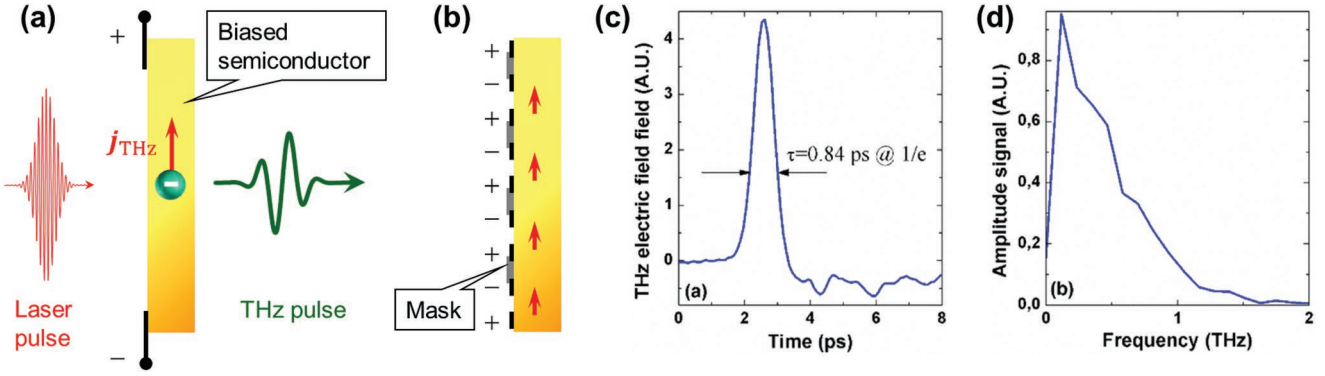

Figure 18. a) Schematic principle of large-area photoconductive emitters. b) Photoconductive emitter with multiple electrodes to reduce the required bias voltage and a mask to prevent destructive interference of emission from gaps of opposite bias. c) THz electric field and d) resulting amplitude spectrum from a large-area ZnSe photoconductive emitter. c,d) Adapted with permission.[102] Copyright 2016, The Optical Society of America.

so-called Reststrahlen band located typically between 1 and 15 THz. This constraint is generally absent in metals as they exhibit a featureless THz refractive index.[107] Several works have demonstrated THz emitters based on metal structures and with a bandwidth of up to 3 THz.[108–110] However, the THz field amplitudes obtained so far[108] suggest that scaled versions are not expected to straightforwardly deliver field strengths suitable for strong-field applications.

We note that all emitter concepts summarized up to this point take advantage exclusively of the charge of the electron. Remarkably, new schemes for the generation of photocurrents become available when the spin of the electron is taken into account, too. Recent implementations of this approach are so-called spintronic THz emitters (STEs) which rely on the conversion of an ultrafast spin photocurrent into a transverse charge current.

3.2.1. Basic Concept

As seen in **Figure 19**, the basic STE is a bilayer made of a ferromagnetic (F) and a nonmagnetic (N) metal thin-film. An optical femtosecond pump pulse, incident through the optically transparent substrate, generates a distribution of nonequilibrium electrons in the metal stack. As the transport properties of the majority and minority spins in the F layer differ distinctly, spin transport from the F into the adjacent N layer is launched.[111] When the N layer is made of a heavy metal, spin-orbit coupling can induce substantial spin-dependent deflection of the electrons. This inverse spin Hall effect transforms the out-of-plane spin current into the desired sub-picosecond in-plane charge current that gives rise to the emission of a THz electromagnetic pulse (Figure 19).

The STE concept was recently demonstrated in a number of works (see, e.g., refs. [112–114]). The dependence of the THz amplitude on the N-film thickness indicates that the THz photocurrent flows in a very thin sheet of typically ≈1 to 3 nm thickness close to the F/N interface.[112,115] In a first optimization procedure,[112] the emitted THz amplitude was increased substantially by resorting to very thin films (to increase the excitation density and sheet resistance of the metal), by taking heavy metals such as Pt and W for the N layer (to maximize spin-to-charge-current conversion) and by using W|F|Pt trilayers rather than bilayers (to take advantage of not only forward- but also backward-running spin-polarized electrons).

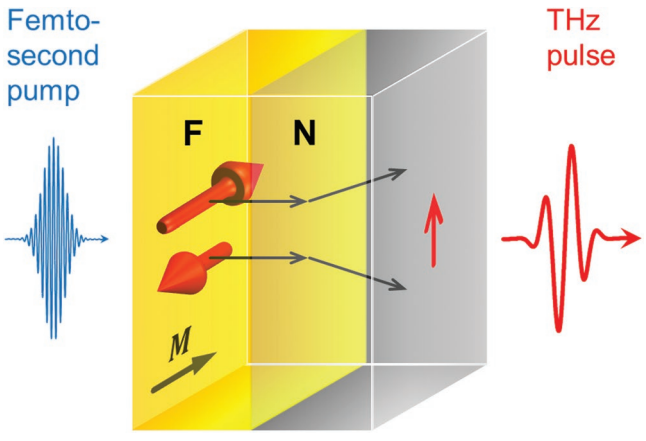

Figure 19. Principle of an STE. The emitter is a stack of a ferromagnetic (F) and a nonmagnetic (N) metal thin film. Excitation with a femtosecond pump pulse triggers spin transport from the F into the N layer where the out-of-plane spin current is converted into an ultrafast in-plane charge current (vertical red arrow). The charge current gives rise to the emission of a THz electromagnetic pulse. The F layer has homogenous magnetization **M** as set by an external magnetic field. Adapted with permission.[112] Copyright 2016, Springer Nature.

The optimized emitter, a W(2 nm)|$Co_{40}Fe_{40}B_{20}$(1.8 nm)|Pt-(2 nm) trilayer on a glass substrate, was excited by laser pulses (energy of 2.5 nJ, duration of 10 fs, center wavelength of 800 nm, repetition rate of 80 MHz) from a Ti:sapphire laser oscillator. The emitted THz pulses gaplessly covered the range from 1 to 30 THz (at 10% of the amplitude maximum) and had peak field substantially exceeding that of reference emitters such as a 1 mm thick (110)-cut ZnTe crystal.[112] Therefore, the STE is particularly interesting for broadband linear spectroscopy,[112,116,117] in particular in the difficult-to-reach range from 5 to 15 THz.

3.2.2. Large-Area Spintronic THz Emitters

It has to be emphasized that fabrication of the spintronic trilayer is inexpensive and straightforward, without involving any lithography steps. Therefore, this emitter concept is easily scalable, making it interesting as a THz source for broadband nonlinear THz spectroscopy. For a first demonstration of this idea, the authors of ref. [118] grew W(1.8 nm)|$Co_{40}Fe_{40}B_{20}$(2 nm)|Pt(1.8 nm) trilayers on a glass substrate with a diameter of 7.5 cm. The emitter costs of ≈20 EUR were dominated by the substrate price, two orders of magnitude less than the current price of (110)-cut ZnTe windows of comparable diameter. To excite the large-scale STE, intense laser pulses (energy of 5.5 mJ, duration of 40 fs, center wavelength of 800 nm, repetition rate of 1 kHz) from an amplified Ti:sapphire laser system were directed onto the STE as a collimated beam (diameter of 4.8 cm). For electro-optic detection, the emitted THz beam was focused onto a ZnTe(110) crystal (thickness of 10 µm).[119,120]

The key result of this study[118] is shown in **Figure 20**a. The transient focal THz electric field was a single-cycle waveform, reached a peak value of approximately 300 kV cm^{-1} and had a duration of 230 fs (full-width at half-maximum of the field envelope, see Figure 20a), consistent with a measured pulse energy of 5 nJ.[118] Note that the THz field spectrum was gapless and spanned the entire range from 0.1 to 10 THz with respect to 10% of the peak spectral amplitude (Figure 20b). The spectral phase was flat and varied by less than $2\pi/10$ (standard deviation), suggesting the THz pulse was nearly bandwidth-limited.

The measured field amplitude of ≈300 kV cm^{-1} is already sufficient to drive quite a number of nonlinear processes, for instance strong-field phenomena such as field ionization of impurities and excitons in semiconductors.[8] As a proof of principle, the authors of ref. [118] used the STE-generated THz pulses (Figure 20) to induce and measure the THz Kerr effect in diamond. The peak amplitude of this first large-area STE was still lower than that produced by mature THz emitters such as those based on $LiNbO_3$ under similar excitation conditions. Nevertheless and compared to other emitter

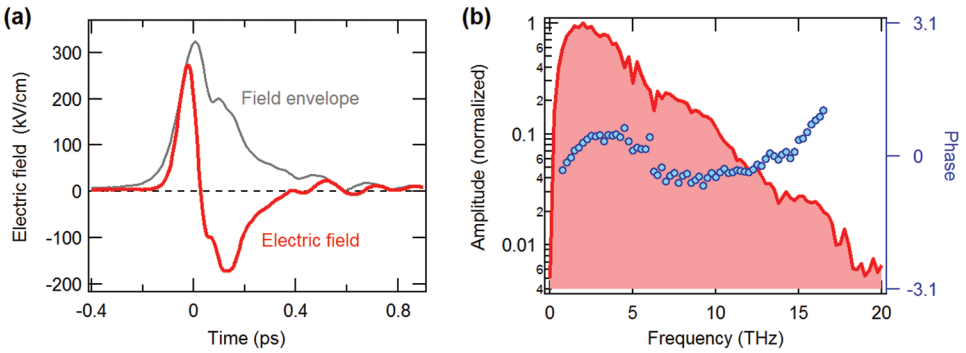

Figure 20. Performance of a large-area STE made of a W(1.8 nm)|$Co_{40}Fe_{40}B_{20}$(2 nm)|Pt(1.8 nm) trilayer on glass (diameter 7.5 cm). a) Transient electric field in the focus of the THz beam along with the field envelope for mJ-class pump pulse (energy of 5.5 mJ, duration of 40 fs, center wavelength of 800 nm, repetition rate of 1 kHz, beam diameter of 4.8 cm). b) Spectral amplitude and phase versus frequency as obtained from the field shown in panel (a). Reproduced with permission.[118] Copyright 2017, AIP Publishing.

concepts, large-area metallic STEs have unique features with significant potential for applications in nonlinear THz spectroscopy:

- The emission spectrum of the large-area STE is broad and gapless (Figure 20b) and approximately comparable to that of plasma sources. The range from 5 to 10 THz is highly interesting for driving resonances of donors in semiconductors[121] and the hydrogen-bond network of water.[122] By shortening the pump-pulse width from 40 to 10 fs, a spectrum covering the full interval from 1 to 30 THz can be expected.[112]
- STE operation is independent of the pump wavelength,[123,124] most likely because the primary function of the pump pulse is heating of the electron subsystem. Therefore, large-scale STEs can be driven by any high-power laser, independent of its output wavelength.
- As the metal stack of the STE is much thinner than all wavelengths involved, no phase-matching issues arise. The thin metal also eases removal of excess heat by the substrate.
- STEs can straightforwardly be used in transmission mode. Because the emitter is thin and relies on a second-order nonlinear optical process, the Gaussian profile of the pump beam is preserved and permits tight focusing.
- Metal thin-film stacks such as the STE are well established, simple, and cheap to fabricate.
- The polarity and the azimuth of the polarization plane of the linearly polarized emitted THz wave can easily be set by the STE's magnetization, which, in turn, can be modulated by an external magnetic field. A completely new and rich parameter space opens up when one takes the step from a homogenous in-plane magnetization of the F layer (Figure 19) to a spatially varying magnetization (**Figure 21**a).

To demonstrate the last feature, Hibberd et al.[114] recently applied a patterned external magnetic field to a large-area STE (Figure 21a) to generate a quadrupole-like THz beam profile (Figure 21b). In the center of the beam focus, the measured transverse THz-field component exhibited a node (Figure 21c) whereas its longitudinal component featured a maximum. A longitudinal field with a peak strength of approximately 18 kV cm^{-1} was generated[114] (Figure 21d), thus demonstrating the potential of STEs for spatiotemporally tailored THz fields.

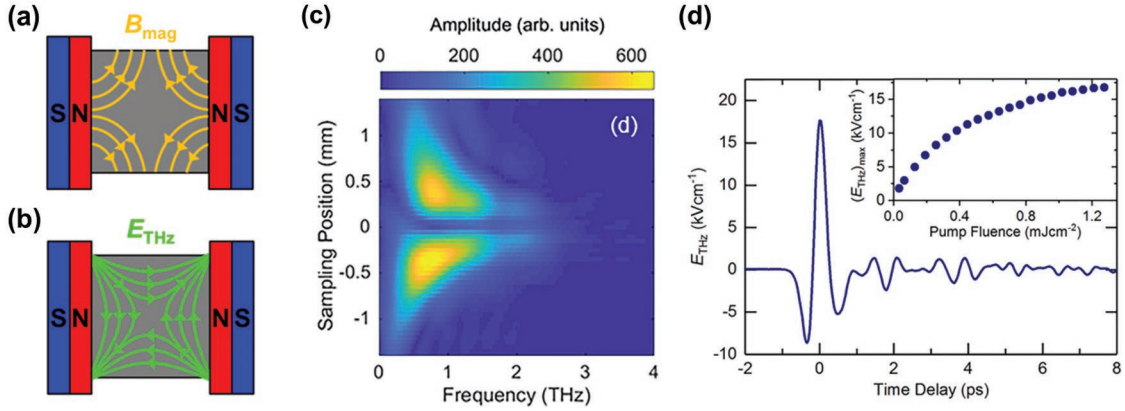

Figure 21. THz polarization control through tailored STE magnetization patterns. a) An inhomogenous magnetic field induces an inhomogenous magnetization distribution and, thus, b) a THz near-field whose shape depends on the magnetization pattern. c) Amplitude spectrum of the transverse field component in the focus of the THz beam as obtained from a large-area STE with the external magnetic-field distribution shown in panel (a). The spectrum was measured as a function of the radial position and displays a minimum in the beam center. d) Measured longitudinal transient THz field in the focus center. Reproduced with permission.[114] Copyright 2019, AIP Publishing.

We finally mention that the development of strong-field STEs is only at the beginning. Numerous improvements can be anticipated, e.g., enhanced pump absorption,[124] optimization of F[125–127] and N materials, better heat dissipation by the substrate, shorter pump pulses,[112] and antenna structures.[128] These options suggest that it should be possible to enter the MV cm^{-1} realm soon. Thus, STEs bear considerable potential for applications in nonlinear THz spectroscopy.

4. THz Sources based on Laser-Filament-Induced Plasmas

Photocurrents can not only be induced in solids, as discussed above, but also in gases, thereby enabling the generation of THz radiation using optically excited gases. Indeed, the first coherent THz radiation from a laser-induced gas plasma was observed by Hamster et al. in 1993.[129] The radiation was driven by ponderomotively induced currents in the plasma, generated using a terawatt laser system. THz pulses generated by a small-scale kHz-repetition-rate regenerative amplifier were demonstrated from the current surge following photoionization of air with an applied DC bias field of about 10 kV cm^{-1}.[130] A significant improvement in efficiency was achieved by mixing femtosecond pulses with their second harmonic (SH) within the gas plasma,[131] while more recently a three-color approach was shown to improve further the efficiency.[132]

A simple schematic of the principle is shown in **Figure 22**. The intense laser pulses produce long plasma strings at the trail of the nonlinear propagation (filamentation), while the combination of the fundamental with the SH (and eventually higher harmonics) results in strong net electron currents that radiate intense THz fields, typically on a conical emission pattern, as will be discussed below.

Originally, as the mechanism of THz generation in plasma driven by a two-color (fundamental and SH) laser field, four-wave frequency mixing (four-wave rectification, FWR) was proposed.[131] Whereas the measured dependence of the THz signal on the relative phase between the fundamental and SH was found to be consistent with an FWR model[131,133,134] (up to a constant phase[135]), the dependence on fundamental intensity was deviating.[131,136] An intensity threshold for THz generation was also observed, proving that generation of plasma is required and the cubic nonlinearity of air is insufficient to explain the measurements.[133,134] The measured strength of the THz field was about four orders of magnitude larger than predicted by FWR using $\chi^{(3)}$, the third-order nonlinear susceptibility of air,[134] indicating a larger optical nonlinearity for the plasma.

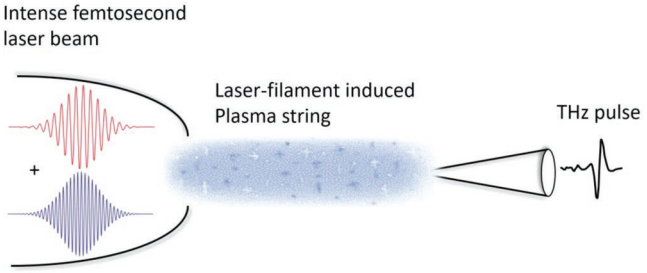

Figure 22. Schematic of the principle of two-color filament-induced THz generation. Intense two-color femtosecond laser pulses generate long plasma strings and strong net electron currents (sensitive to the phase between the harmonics) that radiate intense THz fields, typically on a conical emission pattern.

For a more microscopic description, a semi-classical transient photocurrent model was developed by Kim et al.[135] According to this model, bound electrons undergo tunnel ionization and subsequent coherent motion driven by the two-color laser field

$$E_{\mathrm{L}}(t) = E_{\omega}\cos(\omega t+\varphi) + E_{2\omega}\cos\left[2(\omega t+\varphi)+\vartheta\right] \tag{10}$$

Here, E_{ω} and $E_{2\omega}$ are the fundamental and SH field amplitudes, and ϑ is the relative phase between the two fields. Tunnel ionization is a highly nonlinear process and mainly occurs around the peak of the combined field. The drift velocity of each electron is determined by the phase φ of the field at the instant of ionization. A macroscopic transverse plasma current, oscillating at optical frequencies, is generated in this way. The current contains a nonzero quasi-DC component, which is maximal for $\vartheta = \pi/2$, giving rise to THz emission.

The presence of a plasma current was experimentally confirmed by placing a single-loop wire around the plasma filament (B-dot probe) and measuring the voltage induced by the magnetic field of the current[137] (**Figure 23**). An even more detailed picture of the THz generation process was given by a two-step model.[138] The first step, treated quantum-mechanically by solving the time-dependent Schrödinger equation, is tunnel ionization and the acceleration of the ionized wavepackets by the two-color laser field. The second step, treated analytically, describes Bremsstrahlung as a second source of THz radiation originating from the scattering of the ionized electrons off the neighboring atoms. A detailed analysis of the role of FWR and photocurrents in the generation of THz waves was discussed,[139] showing that although both contributions exist, the plasma one dominates under the filamentation conditions.

A typical experimental realization of two-color-pumped THz generation in gas plasmas is shown in Figure 23a, which also includes a B-dot probe. A femtosecond laser pulse with mJ-level pulse energy, corresponding to powers above the critical level (about 5 GW in air[140]), is focused into a gas target to form a plasma. The SH is generated in a nonlinear crystal, placed between the lens and the focus. As discussed above, the THz generation process is sensitive to the relative phase ϑ between the fundamental and the SH fields. The latter can be adjusted by, e.g., translating the SH generation crystal, utilizing the dispersion of the gas. The THz field polarity can also be controlled (inverted) by changing ϑ by π.[134] The relative directions of fundamental and SH electric field polarizations can be controlled by a dual-band waveplate (Figure 23a), possibly complemented by an additional birefringent plate (not shown in Figure 23a) to compensate accumulated fundamental–SH time delay.[141] The maximum THz signal was found for parallel polarizations of the fundamental and SH.[134] Ambient air, nitrogen, or noble gases can be used as the gas target for plasma generation. THz generation in gas plasmas has the advantage that the pump intensity is not limited by the damage

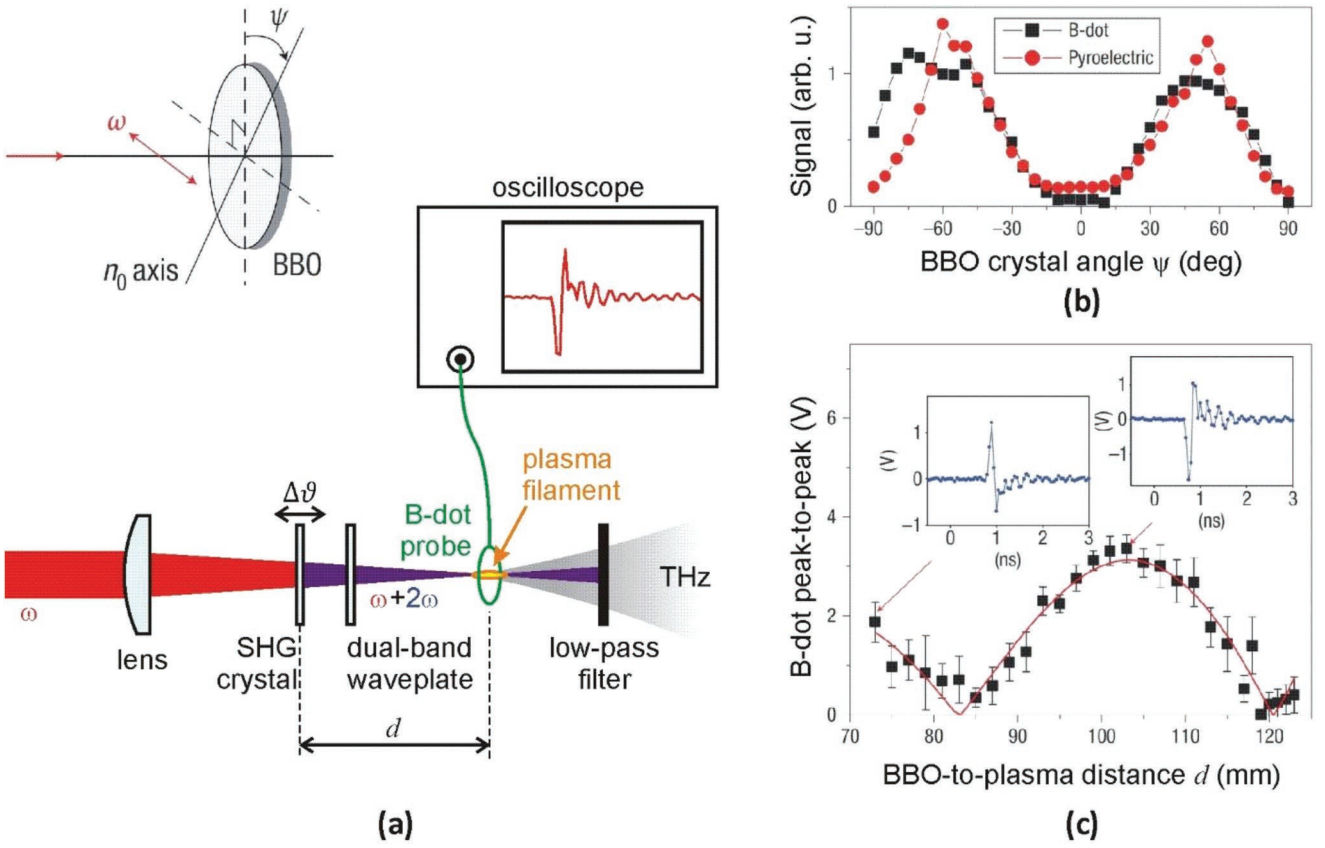

Figure 23. a) Scheme of a two-color laser plasma THz source with a B-dot probe for measuring the transient photocurrent. b) Measured correlation between B-dot and pyroelectric signals as the polarization and intensity of the SH field are varied by rotating the SH-generation crystal as shown in the top left inset in (a). c) B-dot probe voltage signal as a function of SH generation crystal position, demonstrating the dependence of the plasma current on the phase ϑ. Adapted with permission.[137] Copyright 2008, Springer Nature.

threshold of the generating medium. A higher THz generation efficiency can be achieved with noble gases of higher tunnel ionization rate.[137,142] A systematic study of the THz pulse energy and spectrum for varied pump energy and pressure of different gas targets is presented in ref. [142]. Examples of measured waveforms and spectra are shown in **Figure 24**.

The THz radiation generated from laser plasma typically has a broad spectrum, extending from below 1 THz up to about

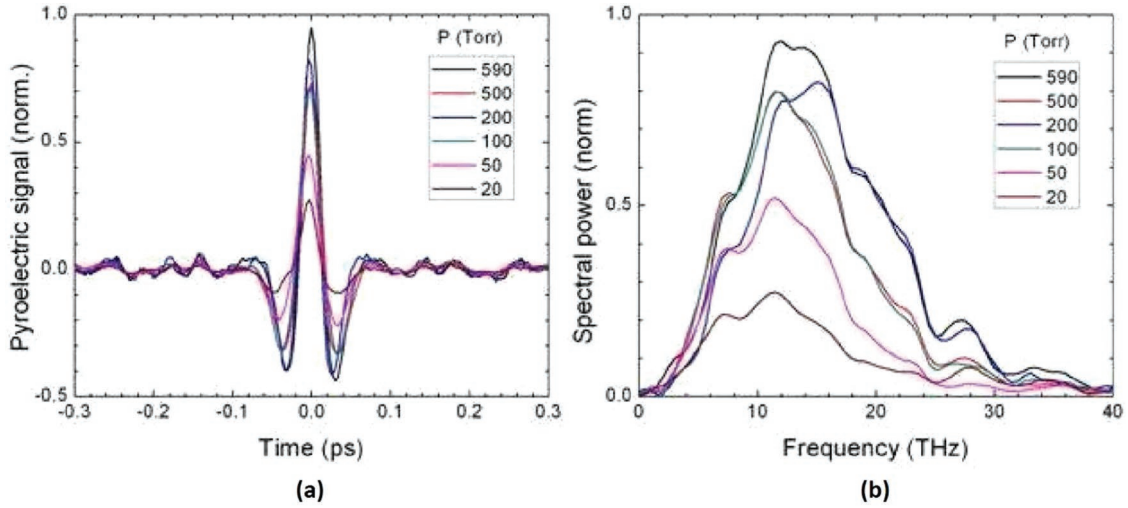

Figure 24. a) Waveforms and b) spectra of THz radiation from air plasma for different gas pressures. Reproduced with permission.[142] Copyright 2010, The Optical Society of America.

40 THz (see, e.g., ref. [142]), or even beyond 100 THz.[143] By focusing a hollow-fiber compressed 10 fs pulse and its SH in air, extremely broad spectra extending up to as high as 200 THz were reported.[144] The bandwidth is limited only by the pulse duration, but not by phonon absorption such as in the case of OR in solids. Pump-to-THz conversion efficiencies up to about 1.5×10^{-4} were reported.[136,137,142] The highest THz pulse energies reported so far, when using 0.8 µm laser filaments, were in the few-µJ range.[145] However, because of the extremely broad THz spectra, peak field strengths up to 8 MV cm^{-1} were reported even for moderate pulse energies.[146]

An interesting way for increasing the optical-to-THz conversion efficiency was suggested using longer pump wavelengths for filamentation.[147] An increase in efficiency by a factor of 30 was demonstrated when pumping at 1.85 µm, as compared to the common 0.8 µm pumping.[147] Yet, at longer wavelengths, and at the limit of 2 µm (available at that time), a drop in the efficiency was observed,[147] discouraging further studies in the following years in this direction. Recently though, a new impetus in the development of powerful mid-infrared laser sources led to new THz studies using longer wavelength drivers. A breakthrough theoretical prediction appeared,[148] suggesting that using a pump laser system at 3.9 µm and its SH, THz conversion efficiency of about 7% can be achieved, more than two orders of magnitude larger compared to 0.8 µm. The projected multi-millijoule THz pulse energies and the short pulse durations lead to focused electric and magnetic field strengths in the GV cm^{-1} and the hundreds-of-tesla regime, respectively (**Figure 25**), opening the way to extreme nonlinear THz science. The first experimental demonstration of such high conversion efficiency was reported recently.[149] A theoretical parametric study as a function of the driving laser wavelength, from the near to the far infrared,[150] as well as an experimental one up to 2.6 µm,[151] confirms that the use of long wavelength short pulses, above critical power, results in energetic THz pulses. The increased efficiency can be understood as the result of stronger photocurrents from the bigger ponderomotive forces and the contribution of the filament-induced multiple harmonics.[148]

The THz radiation generated by a two-color plasma filament has a conical emission pattern, a feature characteristic

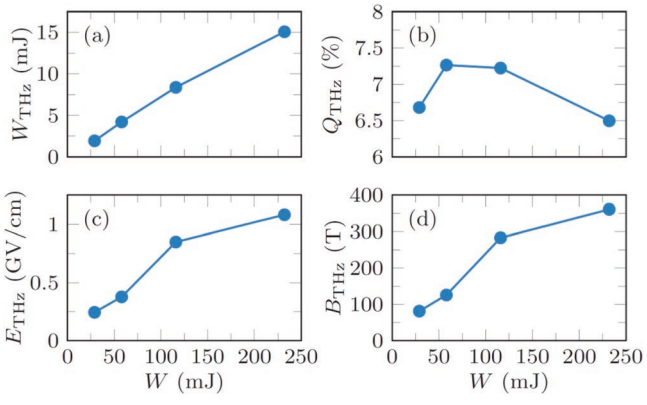

Figure 25. a) THz pulse energy W_{THz}, b) THz conversion efficiency Q_{THz}, c) estimated peak electric E_{THz} field, and d) magnetic field B_{THz} of focused THz pulses as functions of the input energy W of 3.9 µm two-color laser pulses. Reproduced with permission.[148] Copyright 2018, American Physical Society.

especially for long filaments. The reason is off-axis phase matching.[152] In the forward (on-axis) direction the effective length for THz generation is limited to $L_{eff} = (\lambda_p/2)/(n_\omega - n_{2\omega}) \approx 22$ mm in ambient air, over which the polarity of the THz pulse remains unchanged. This length corresponds to a fundamental-to-SH relative phase shift of $\vartheta(L_{eff}) - \vartheta_0 = \pi$. Here, n_ω and $n_{2\omega}$ are the refractive indices of the plasma filament at the fundamental and SH frequencies, respectively. At off-axis angles, phase matching over much larger distances can be fulfilled, resulting in the conical emission pattern with typical opening angles in the range of 2° to 10°.[145,152,153]

The conical emission can be a drawback in some applications, especially when the cone angle is big. It has been shown though[150] that the THz conical emission angle reduces with increase of the driving laser wavelength, making the THz radiation better directed and easier to collect. Another way to circumvent this problem and/or the limitation set by group velocity dispersion, is the use of plasma sheets, created using cylindrical lenses, instead of filaments.[145]

Beyond the gas laser-plasma sources, THz laser-plasma approaches from liquids and solids have also been proposed with exciting properties. Although most liquids, like water, strongly absorb THz radiation, demonstrations of using these as sources have been performed. One way is to limit the propagation effects by confining the liquid in space, like in the case of water films[154] or water lines.[155] These approaches offer conversion efficiencies that are significantly higher than single-color laser-plasmas in gases, but do not perform better than two-color ones in gases, especially since the obtained THz bandwidths are much narrower and, thus, the pulse durations are much longer. The other way that has been proposed is long single-color filamentation in water cells.[156] THz pulse energies up to 80 µJ were obtained when pumping with about 30 mJ at 0.8 µm, while the THz pulse bandwidths reached 100 THz. The mechanism that leads to these intense THz fields are strong photocurrents that are created during the nonlinear propagation, because of an in-phase SH component from the supercontinuum that is produced along the propagation.[156]

Finally, a more exotic laser-plasma technique for THz generation in a laser-driven ion accelerator using solid targets has been reported. THz pulses with 460 µJ energy were reported by irradiating thin metal foil targets with 600 mJ laser pulses focused to intensities up to 5×10^{19} W cm^{-2}.[157] Generation of THz radiation was explained by the presence of transient currents at the target rear surface. Recently, using 60 J of laser energy, tens-of-mJ THz pulse energies could be achieved from a similar source.[158] The strong THz emission is attributed to coherent transition radiation, induced by the laser-accelerated energetic electron bunch escaping the target.

The extremely broad bandwidth of THz pulses from plasma generated by two-color laser fields requires broadband detection techniques. Common electro-optic crystals are not always suitable because their transfer function can exhibit significant variations in amplitude and phase, in particular around the Reststrahlen band.[119] An alternative is THz air-biased coherent detection: SH generation of the fundamental laser field by four-wave frequency mixing in the gas, involving the THz field and an AC bias, can be used to measure the temporal dependence

of the THz electric field.[4,138] The broadband detection of THz waves in gases has even been extended to THz remote sensing by coherently manipulating the (UV) fluorescence emission from an asymmetrically ionized gas plasma,[159] or even through the THz enhancement of acoustic waves.[160]

5. Emerging Applications

Intense THz pulses can drive selected degrees of freedom in matter into regimes far beyond the small-perturbation limit. This feature has enabled new applications that can roughly be classified in terms of nonlinear spectroscopy (providing insights into the nature of the driven mode) and materials control (driving the system into a target state). The response of the system is usually probed by a time-delayed probe pulse of suitable photon energy. These ideas are briefly outlined in the following. It should be emphasized that the overview provided here is very brief and, thus, certainly incomplete, highlighting only a few illustrative examples. More detailed reviews on nonlinear light-matter interaction at THz frequencies can be found, e.g., in refs. [3–6,8–13].

5.1. Nonlinear THz Spectroscopy

5.1.1. Properties of Driven Modes

THz radiation enables resonant excitation of fundamental motions such as phonons, electron intraband transport, and magnons. Driving these modes to large amplitudes can enable new insights into their properties. For instance, excitation of infrared-optical phonons with intense THz pulses and tracing the anharmonic response[161] allowed one to reconstruct the atomic-scale potential the ions are moving in.[162,163] Even if the phonon of interest is infrared-inactive yet Raman-active does THz radiation provide new means of phonon excitation by a Raman-type sum-frequency process.[164] Here, two frequencies of the incident THz pulse induce a force on the lattice oscillating at the sum frequency, rather than the difference frequency that occurs in standard Raman-type excitations. By using intense THz pulses centered at 20 THz, Raman-active zone-center optical phonons of diamond at a frequency of 40 THz were successfully excited and phase-coherently controlled.[164] This process can also be considered as 2PA by an optical transition between two adjacent vibrational levels.

In polar solvents, an incident THz field can directly couple to reorientational molecular motions through the permanent molecular dipole moments. Accordingly, it was shown that intense THz pulses align solvent molecules more efficiently than optical fields do.[165,166] By comparing optically driven with THz-driven alignment, it was determined whether or whether not rotational molecular degrees of freedom make a dominant contribution to the dielectric function of polar solvents such as methanol.[167]

Strong THz fields are ideally suited to drive nonlinear electron transport in solids, which often results in the reemission of radiation with new frequencies[168] such as higher harmonics, e.g., in semiconductors,[169] graphene,[170] and superconductors.[171,172] Analysis of the reemitted THz field often allows one to reconstruct the dynamics of the THz-induced current, thereby providing important information on the mechanism from which it arises.[168,169]

Finally, by using intense THz magnetic and electric fields, nonlinear magnetic responses of magnetically ordered solids were observed, thereby providing insights into the underlying effective spin Hamiltonian,[173] the relative impact of electric and magnetic field component of the THz pulse,[174] and the magnetooptic probing mechanism.[175]

5.1.2. Interaction between Modes

Generally, nonlinear THz spectroscopy allows one to probe the interaction of the driven mode with other modes of the system. An implementation of this approach is 2D THz spectroscopy[8,10,11,176] in which the sample response to two intense THz pulses as a function of the delay between these pulses is measured. Examples include magnon–magnon interactions,[177] electron–phonon coupling in semiconductors[178,179] and superconductors,[11] and the coupling of collective nuclear modes of solvents such as water.[122,180]

In particular, to reveal interactions between the crystal lattice and spins in magnetically ordered solids, one can make use of the generic pump-probe scheme shown in **Figure 26**.[21,22] An intense THz pump pulse is used to resonantly excite optical phonons. The impact on the spin subsystem is monitored by measuring the transient Faraday effect, potentially over multiple time scales from femtoseconds to milliseconds.[22] By applying this scheme to the rare-earth orthoferrite $ErFeO_3$, a new coupling channel through anharmonic phonon coupling was discovered.[21] In the model insulating ferrimagnet YIG, the equilibration of crystal lattice and spins was revealed and shown to proceed on distinctly different time scales as fast as 1 ps (in terms of energy exchange) and as slow as 100 ns (in terms of angular-momentum exchange).[22]

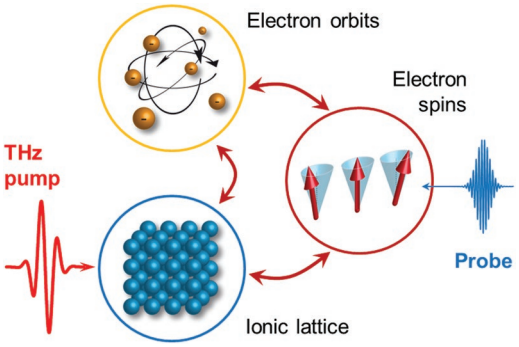

Figure 26. Schematic of a mode-specific THz-pump optical-probe experiment. A THz pump pulse selectively excites a resonant mode (here an optical phonon). Subsequently, the resulting dynamics of other degrees of freedom (here the subsystem of electron spins) are probed by a suitable (here magnetooptic) probe pulse. Reproduced with permission.[22] Copyright 2018, The Author(s). Some rights reserved; exclusive licensee AAAS. Distributed under CC BY-NC 4.0.

5.2. THz Materials Control

5.2.1. Condensed Matter

Intense THz pulses have been shown to be highly promising stimuli to switch materials between macroscopic states, e.g., VO_2[181] or the manganite $Pr_{0.7}Ca_{0.3}MnO_3$[182] from an insulating to a conductive phase or the direction of ordered spins in antiferromagnets.[18,19] A particularly interesting case of switching occurs when the new phase is a "hidden state," i.e., a metastable and, thus, transient state of matter. Examples of such states include transient ferroelectric order in a paraelectric,[183,184] transient superconductivity-like states in superconductors in the normal-conductor phase,[185] and the heating of the spin system of a ferrimagnet without changing its total magnetization (see also Figure 26).[22]

5.2.2. Free Charged Particles

Another remarkable example of THz control over matter, the efficient manipulation of free charged particles and their (relativistic) beams requires THz field strengths on the order of 1–10 MV cm^{-1}, in some cases even 100 MV cm^{-1}. The enhancement of attosecond-pulse generation by manipulating laser-ionized electron trajectories in high-harmonic generation in gases has been studied theoretically.[186,187] THz-field-induced electron emission has been shown from flat metal surface[188] and metal nanostructures.[189–191] Electron acceleration, undulation, deflection, and spatial as well as temporal focusing with THz fields has been proposed.[192] Focused beams of counterpropagating THz pulse pairs have been proposed both for acceleration and longitudinal bunch compression.[193] In the first proof-of-principle experiment of THz-driven electron acceleration, 7 keV energy gain was demonstrated in a mm-sized dielectric-loaded cylindrical metallic waveguide, driven by 10 µJ THz pulses.[23] In segmented THz electron accelerator and manipulator (STEAM) structures (**Figure 27**a),[194] acceleration with 70 keV energy gain,[195] bunch compression to 100 fs,[194,195] as well as deflection and focusing have been achieved.[194]

Using THz radiation for acceleration can be superior to conventional microwave-based technologies in several ways. First, THz pulses can be generated with significantly smaller temporal jitter to the electron bunch to be manipulated, or to other ultrashort optical pulses to be used in pump-probe experiments. Second, the higher frequencies and shorter pulses in the THz range are beneficial for a higher maximum acceleration gradient, which is limited by field-induced breakdown and scales with the sixth power of the field duration (see ref. [194]. and references therein). For example, by using THz pulses with mJ-scale energy, GeV m^{-1} accelerating gradient and electron energies on the 10 MeV scale can be expected.[23] Third, electron bunches as short as a few fs, or even sub-fs, can be produced by THz compression and acceleration.[194]

GeV m^{-1} accelerating gradients can be achieved by wakefield acceleration in a laser plasma driven by TW–PW scale lasers, but this technique is susceptible to instabilities. Direct acceleration by intense optical fields is also possible. However, due to the short optical wavelength, it is challenging to achieve a sufficiently precise synchronization of the electron bunch to the laser field, the bunch charge is limited, and structure manufacturing is difficult.

The generation of ultrashort electron bunches with large (pC) charge requires very large electric field strengths to reduce the space-charge effects in the initial acceleration stage. Recently, a THz-driven electron gun was demonstrated with promising scaling potential.[196,197] For initial acceleration stages, schemes supporting sub-luminal THz propagation can be also advantageous.[198] Expectedly, table-top THz-driven electron sources with relativistic energies and high charge density will soon become available for important applications, such as ultrafast electron microscopy and diffraction.[199]

Postacceleration of laser-generated proton beams has also been proposed.[17] It utilizes the evanescent field of THz pulses in the vacuum gap between a pair of dielectric crystals (Figure 27b). Laser-driven accelerators typically produce ion beams with up to a few tens of MeV energies per nucleon and

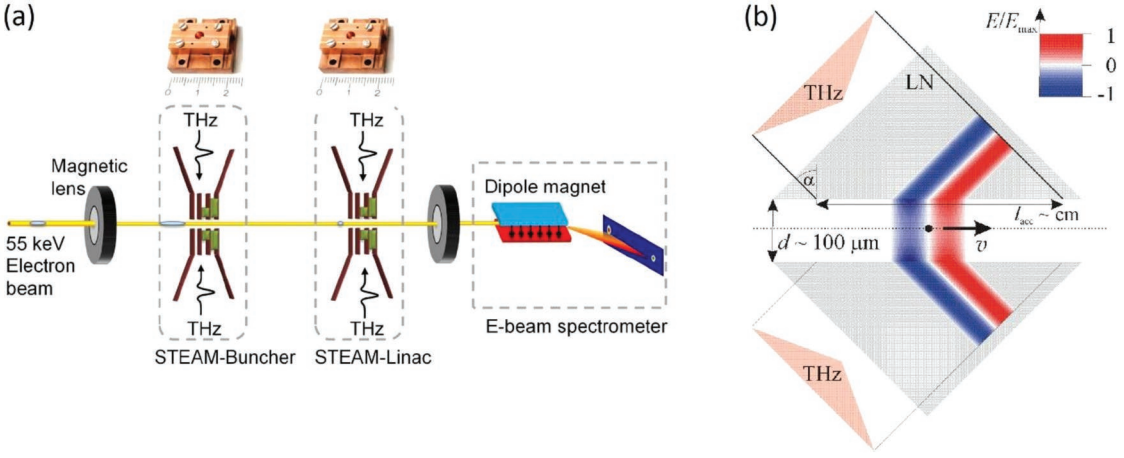

Figure 27. a) Concept of a segmented THz electron accelerator and manipulator (STEAM) for producing tailored ultrashort electron bunches. Reproduced with permission.[195] Copyright 2019, The Optical Society of America. b) Scheme of the evanescent-wave postaccelerator for laser-generated proton beams. Reproduced under the terms of the Creative Commons Attribution 3.0 License.[17] Copyright 2014, American Physical Society.

extremely broad energy spectra. It is predicted that the energy of a laser-generated proton bunch can be increased from 40 to 56 MeV in five subsequent THz-driven postaccelerator stages, and its initial broad energy distribution can be significantly reduced. For this application, THz pulses in the 0.1 to 0.5 THz frequency range and with a peak electric field on the MV cm^{-1} level are particularly suitable,[17] similar to those reported in ref. [63]. These features hold promise for compact ion accelerators, suitable even for hadron therapy. Another recent proposal is a THz-driven ion source from a near-critical-density hydrogen plasma.[16]

6. Conclusion

There has been a rapid progress in the last decade in the technologies of generating intense ultrashort THz pulses in all parts of the THz spectrum (0.1 to ≈100 THz). An overview of femtosecond-laser-based technologies has been given. In terms of OR, the emphasis was on lithium niobate, semiconductors, and organic crystals. Tilted-pulse-front pumping, in combination with novel easily scalable concepts such as the nonlinear echelon slab or the CG, will enable to reach unprecedented THz pulse energies and field strengths on the multi-10 MV cm^{-1} scale. DFG and OPA are already delivering such extremely high fields at higher THz frequencies.

Solid-state photocurrent emitters have been discussed, where photoconductive antennas and STEs have recently demonstrated potential for generating intense THz fields and flexible polarization engineering capabilities in the latter case. THz sources based on (two-color) laser-filamentation-induced plasmas can cover an extremely broad spectral range and show exciting perspective for increasing the field strength by using longer infrared pump wavelengths.

Further progress in all of these technologies can be expected in the near future, pushing the limits of achievable THz pulse energies, peak electric, and magnetic field strengths to the extremely strong-field and even to the relativistic regime. THz pulses with MV cm^{-1}-scale field strength have been extensively used recently for nonlinear THz spectroscopy. Cutting-edge THz sources are now enabling new classes of applications: nonlinear THz spectroscopy and THz strong-field control over matter such as the efficient manipulation and acceleration of charged particles. THz-driven compact particle accelerators are expected to revolutionize accelerator technology and its applications in materials science, biology, and medicine.

Acknowledgements

Helpful discussion with János Hebling is acknowledged. J.A.F. acknowledges funding from National Research, Development and Innovation Office (NKFIH) (NN 125808, 2018-1.2.1-NKP-2018-00009, 2018-1.2.1-NKP-2018-00010) and from the European Union and NKFIH (E 12576 HABRIA, 2018-2.1.5-NEMZ-2018-00003). S.T. acknowledges funding through the projects NPRP9-329-1-067 of the Qatar National Research Fund (member of The Qatar Foundation), H2020 Laserlab-Europe (EC-GA 654148), H2020 MIR-BOSE (EC-GA 737017), and "HELLAS-CH" (MIS 5002735) co-financed by Greece and the European Union. T.K. acknowledges funding through the projects ERC H2020 CoG TERAMAG (grant no.: 681917) and DFG TRR227 Ultrafast Spin Dynamics (B02).

Conflict of Interest

The authors declare no conflict of interest.

Keywords

optical rectification, plasma-based terahertz sources, spintronic emitters, strong-field terahertz–matter interactions, terahertz pulses

Received: April 23, 2019
Revised: September 9, 2019
Published online: December 3, 2019

[1] R. Ulbricht, E. Hendry, J. Shan, T. F. Heinz, M. Bonn, *Rev. Mod. Phys.* **2011**, *83*, 543.
[2] P. U. Jepsen, D. G. Cooke, M. Koch, *Laser Photonics Rev.* **2011**, *5*, 124.
[3] J. Hebling, K. L. Yeh, M. C. Hoffmann, K. A. Nelson, *IEEE J. Sel. Top. Quantum Electron.* **2008**, *14*, 345.
[4] M. C. Hoffmann, J. A. Fülöp, *J. Phys. D: Appl. Phys.* **2011**, *44*, 083001.
[5] K. Tanaka, H. Hirori, M. Nagai, *IEEE Trans. Terahertz Sci. Technol.* **2011**, *1*, 301.
[6] M. C. Hoffmann, in *Terahertz Spectroscopy and Imaging* (Eds: K.-E. Peiponen, A. Zeitler, M. Kuwata-Gonokami), Springer, Berlin, Heidelberg **2013**.
[7] N. Stojanovic, M. Drescher, *J. Phys. B: At., Mol. Opt. Phys.* **2013**, *46*, 192001.
[8] T. Kampfrath, K. Tanaka, K. A. Nelson, *Nat. Photonics* **2013**, *7*, 680.
[9] A. Pashkin, F. Junginger, B. Mayer, C. Schmidt, O. Schubert, D. Brida, R. Huber, A. Leitenstorfer, *IEEE J. Sel. Top. Quantum Electron.* **2013**, *19*, 8401608.
[10] H. Y. Hwang, S. Fleischer, N. C. Brandt, B. G. Perkins, M. Liu, K. Fan, A. Sternbach, X. Zhang, R. D. Averitt, K. A. Nelson, *J. Mod. Opt.* **2015**, *62*, 1447.
[11] D. Nicoletti, A. Cavalleri, *Adv. Opt. Photonics* **2016**, *8*, 401.
[12] H. A. Hafez, X. Chai, A. Ibrahim, S. Mondal, D. Férachou, X. Ropagnol, T. Ozaki, *J. Opt.* **2016**, *18*, 093004.
[13] D. M. Mittleman, *J. Appl. Phys.* **2017**, *122*, 230901.
[14] T. Qi, Y.-H. Shin, K.-L. Yeh, K. A. Nelson, A. M. Rappe, *Phys. Rev. Lett.* **2009**, *102*, 247603.
[15] S. Wienholdt, D. Hinzke, U. Nowak, *Phys. Rev. Lett.* **2012**, *108*, 247207.
[16] A. Sharma, Z. Tibai, J. Hebling, *Phys. Plasmas* **2016**, *23*, 063111.
[17] L. Pálfalvi, J. A. Fülöp, G. Tóth, J. Hebling, *Phys. Rev. Spec. Top.–Accel. Beams* **2014**, *17*, 031301.
[18] K. Olejník, T. Seifert, Z. Kašpar, V. Novák, P. Wadley, R. P. Campion, M. Baumgartner, P. Gambardella, P. Němec, J. Wunderlich, J. Sinova, P. Kužel, M. Müller, T. Kampfrath, T. Jungwirth, *Sci. Adv.* **2018**, *4*, eaar3566.
[19] S. Schlauderer, C. Lange, S. Baierl, T. Ebnet, C. P. Schmid, D. C. Valovcin, A. K. Zvezdin, A. V. Kimel, R. V. Mikhaylovskiy, R. Huber, *Nature* **2019**, *569*, 383.
[20] A. Cartella, T. F. Nova, M. Fechner, R. Merlin, A. Cavalleri, *Proc. Natl. Acad. Sci. U. S. A.* **2018**, *115*, 12148.
[21] T. F. Nova, A. Cartella, A. Cantaluppi, M. Först, D. Bossini, R. V. Mikhaylovskiy, A. V. Kimel, R. Merlin, A. Cavalleri, *Nat. Phys.* **2017**, *13*, 132.

[22] S. F. Maehrlein, I. Radu, P. Maldonado, A. Paarmann, M. Gensch, A. M. Kalashnikova, R. V. Pisarev, M. Wolf, P. M. Oppeneer, J. Barker, T. Kampfrath, *Sci. Adv.* **2018**, *4*, eaar5164.
[23] E. A. Nanni, W. R. Huang, K.-H. Hong, K. Ravi, A. Fallahi, G. Moriena, R. J. Dwayne Miller, F. X. Kärtner, *Nat. Commun.* **2015**, *6*, 8486.
[24] L. Novotny, B. Hecht, *Principles of Nano-optics*, Cambridge University Press, Cambridge **2012**.
[25] R. Resta, D. Vanderbilt, in *Physics of Ferroelectrics: A Modern Perspective*, Springer, Berlin, Heidelberg **2007**.
[26] R. W. Boyd, *Nonlinear Optics*, Academic Press, Amsterdam; Boston, MA **2008**.
[27] D. H. Auston, *Appl. Phys. Lett.* **1983**, *43*, 713.
[28] D. H. Auston, K. P. Cheung, J. A. Valdmanis, D. A. Kleinman, *Phys. Rev. Lett.* **1984**, *53*, 1555.
[29] K. Wynne, J. J. Carey, *Opt. Commun.* **2005**, *256*, 400.
[30] J. R. Morris, Y. R. Shen, *Opt. Commun.* **1971**, *3*, 81.
[31] K. H. Yang, P. L. Richards, Y. R. Shen, *Appl. Phys. Lett.* **1971**, *19*, 320.
[32] K. L. Vodopyanov, *Opt. Express* **2006**, *14*, 2263.
[33] R. L. Sutherland, D. G. McLean, S. Kirkpatrick, *Handbook of Nonlinear Optics*, Marcel Dekker, New York **2003**.
[34] Q. Wu, X. C. Zhang, *Appl. Phys. Lett.* **1996**, *68*, 1604.
[35] J. Hebling, A. G. Stepanov, G. Almási, B. Bartal, J. Kuhl, *Appl. Phys. B: Lasers Opt.* **2004**, *78*, 593.
[36] J. Hebling, K.-L. Yeh, M. C. Hoffmann, B. Bartal, K. A. Nelson, *J. Opt. Soc. Am. B* **2008**, *25*, B6.
[37] J. A. Fülöp, L. Pálfalvi, G. Almási, J. Hebling, *Opt. Express* **2010**, *18*, 12311.
[38] J.-H. Jeong, B.-J. Kang, J.-S. Kim, M. Jazbinsek, S.-H. Lee, S.-C. Lee, I.-H. Baek, H. Yun, J. Kim, Y. S. Lee, J.-H. Lee, J.-H. Kim, F. Rotermund, O. P. Kwon, *Sci. Rep.* **2013**, *3*, 3200.
[39] M. C. Hoffmann, K.-L. Yeh, J. Hebling, K. A. Nelson, *Opt. Express* **2007**, *15*, 11706.
[40] T. Hattori, K. Takeuchi, *Opt. Express* **2007**, *15*, 8076.
[41] M. Jewariya, M. Nagai, K. Tanaka, *J. Opt. Soc. Am. B* **2009**, *26*, A101.
[42] K. Ravi, W. R. Huang, S. Carbajo, X. Wu, F. Kärtner, *Opt. Express* **2014**, *22*, 20239.
[43] J. Hebling, G. Almási, I. Z. Kozma, J. Kuhl, *Opt. Express* **2002**, *10*, 1161.
[44] F. Blanchard, B. E. Schmidt, X. Ropagnol, N. Thiré, T. Ozaki, R. Morandotti, D. G. Cooke, F. Légaré, *Appl. Phys. Lett.* **2014**, *105*, 241106.
[45] J. A. Fülöp, G. Polónyi, B. Monoszlai, G. Andriukaitis, T. Balciunas, A. Pugzlys, G. Arthur, A. Baltuska, J. Hebling, *Optica* **2016**, *3*, 1075.
[46] G. Polónyi, B. Monoszlai, G. Gäumann, E. J. Rohwer, G. Andriukaitis, T. Balciunas, A. Pugzlys, A. Baltuska, T. Feurer, J. Hebling, J. A. Fülöp, *Opt. Express* **2016**, *24*, 23872.
[47] J. A. Fülöp, J. Hebling, in *Recent Optical and Photonic Technologies* (Ed: K. Y. Kim), InTech, Rijeka **2010**.
[48] J. Hebling, *Opt. Quantum Electron.* **1996**, *28*, 1759.
[49] O. E. Martinez, J. P. Gordon, R. L. Fork, *J. Opt. Soc. Am. A* **1984**, *1*, 1003.
[50] J.-C. Diels, W. Rudolph, *Ultrashort Laser Pulse Phenomena: Fundamentals, Techniques, and Applications on a Femtosecond Time Scale*, Elsevier/Academic Press, Amsterdam; Boston, MA **2006**.
[51] L. Pálfalvi, J. Hebling, J. Kuhl, Á. Péter, K. Polgár, *J. Appl. Phys.* **2005**, *97*, 123505.
[52] B. Bartal, I. Z. Kozma, A. G. Stepanov, G. Almási, J. Kuhl, E. Riedle, J. Hebling, *Appl. Phys. B* **2007**, *86*, 419.
[53] L. Pálfalvi, J. Hebling, G. Almási, Á. Péter, K. Polgár, K. Lengyel, R. Szipöcs, *J. Appl. Phys.* **2004**, *95*, 902.
[54] A. G. Stepanov, J. Hebling, J. Kuhl, *Appl. Phys. Lett.* **2003**, *83*, 3000.
[55] A. G. Stepanov, J. Kuhl, I. Z. Kozma, E. Riedle, G. Almási, J. Hebling, *Opt. Express* **2005**, *13*, 5762.
[56] K. L. Yeh, M. C. Hoffmann, J. Hebling, K. A. Nelson, *Appl. Phys. Lett.* **2007**, *90*, 171121.
[57] A. G. Stepanov, S. Henin, Y. Petit, L. Bonacina, J. Kasparian, J. P. Wolf, *Appl. Phys. B* **2010**, *101*, 11.
[58] H. Hirori, A. Doi, F. Blanchard, K. Tanaka, *Appl. Phys. Lett.* **2011**, *98*, 091106.
[59] M. Sajadi, M. Wolf, T. Kampfrath, *Opt. Express* **2015**, *23*, 28985.
[60] X.-J. Wu, J.-L. Ma, B.-L. Zhang, S.-S. Chai, Z.-J. Fang, C.-Y. Xia, D.-Y. Kong, J.-G. Wang, H. Liu, C.-Q. Zhu, X. Wang, C.-J. Ruan, Y.-T. Li, *Opt. Express* **2018**, *26*, 7107.
[61] L. Pálfalvi, J. A. Fülöp, G. Almási, J. Hebling, *Appl. Phys. Lett.* **2008**, *92*, 171107.
[62] J. A. Fülöp, L. Pálfalvi, S. Klingebiel, G. Almási, F. Krausz, S. Karsch, J. Hebling, *Opt. Lett.* **2012**, *37*, 557.
[63] J. A. Fülöp, Z. Ollmann, C. Lombosi, C. Skrobol, S. Klingebiel, L. Pálfalvi, F. Krausz, S. Karsch, J. Hebling, *Opt. Express* **2014**, *22*, 20155.
[64] J. A. Fülöp, L. Pálfalvi, M. C. Hoffmann, J. Hebling, *Opt. Express* **2011**, *19*, 15090.
[65] S.-W. Huang, E. Granados, W. R. Huang, K.-H. Hong, L. E. Zapata, F. X. Kärtner, *Opt. Lett.* **2013**, *38*, 796.
[66] C. Lombosi, G. Polónyi, M. Mechler, Z. Ollmann, J. Hebling, J. A. Fülöp, *New J. Phys.* **2015**, *17*, 083041.
[67] Z. Ollmann, J. Hebling, G. Almási, *Appl. Phys. B* **2012**, *108*, 821.
[68] M. Tsubouchi, K. Nagashima, F. Yoshida, Y. Ochi, M. Maruyama, *Opt. Lett.* **2014**, *39*, 5439.
[69] L. Pálfalvi, Z. Ollmann, L. Tokodi, J. Hebling, *Opt. Express* **2016**, *24*, 8156.
[70] L. Pálfalvi, G. Tóth, L. Tokodi, Z. Márton, J. A. Fülöp, G. Almási, J. Hebling, *Opt. Express* **2017**, *25*, 29560.
[71] P. S. Nugraha, G. Krizsán, C. Lombosi, L. Pálfalvi, G. Tóth, G. Almási, J. A. Fülöp, J. Hebling, *Opt. Lett.* **2019**, *44*, 1023.
[72] G. Tóth, L. Pálfalvi, J. A. Fülöp, G. Krizsán, N. H. Matlis, G. Almási, J. Hebling, *Opt. Express* **2019**, *27*, 7762.
[73] B. K. Ofori-Okai, P. Sivarajah, W. Ronny Huang, K. A. Nelson, *Opt. Express* **2016**, *24*, 5057.
[74] S. W. Jolly, N. H. Matlis, F. Ahr, V. Leroux, T. Eichner, A.-L. Calendron, H. Ishizuki, T. Taira, F. X. Kärtner, A. R. Maier, *Nat. Commun.* **2019**, *10*, 2591.
[75] F. Blanchard, L. Razzari, H. C. Bandulet, G. Sharma, R. Morandotti, J. C. Kieffer, T. Ozaki, M. Reid, H. F. Tiedje, H. K. Haugen, F. A. Hegmann, *Opt. Express* **2007**, *15*, 13212.
[76] F. Junginger, A. Sell, O. Schubert, B. Mayer, D. Brida, M. Marangoni, G. Cerullo, A. Leitenstorfer, R. Huber, *Opt. Lett.* **2010**, *35*, 2645.
[77] A. Sell, A. Leitenstorfer, R. Huber, *Opt. Lett.* **2008**, *33*, 2767.
[78] P. S. Nugraha, G. Krizsán, G. Polónyi, M. I. Mechler, J. Hebling, G. Tóth, J. A. Fülöp, *J. Phys. B: At., Mol. Opt. Phys.* **2018**, *51*, 094007.
[79] P. Y. Yu, M. Cardona, *Fundamentals of Semiconductors: Physics and Materials Properties*, Springer, Berlin; New York **2010**.
[80] T. Löffler, T. Hahn, M. Thomson, F. Jacob, H. G. Roskos, *Opt. Express* **2005**, *13*, 5353.
[81] G. Chang, C. J. Divin, J. Yang, M. A. Musheinish, S. L. Williamson, A. Galvanauskas, T. B. Norris, *Opt. Express* **2007**, *15*, 16308.
[82] S. A. Ku, C. M. Tu, W. C. Chu, C. W. Luo, K. H. Wu, A. Yabushita, C. C. Chi, T. Kobayashi, *Opt. Express* **2013**, *21*, 13930.
[83] Z. Ollmann, J. A. Fülöp, J. Hebling, G. Almási, *Opt. Commun.* **2014**, *315*, 159.
[84] P. Malevich, G. Andriukaitis, T. Flöry, A. J. Verhoef, A. Fernández, S. Ališauskas, A. Pugžlys, A. Baltuška, L. H. Tan, C. F. Chua, P. B. Phua, *Opt. Lett.* **2013**, *38*, 2746.
[85] G. Polónyi, M. I. Mechler, J. Hebling, J. A. Fülöp, *IEEE J. Sel. Top. Quantum Electron.* **2017**, *23*, 1.
[86] G. Tóth, J. A. Fülöp, J. Hebling, *Opt. Express* **2017**, *25*, 28258.

[87] I. M. Bayanov, R. Danielius, P. Heinz, A. Seilmeier, *Opt. Commun.* **1994**, *113*, 99.
[88] X. C. Zhang, X. F. Ma, Y. Jin, T. M. Lu, E. P. Boden, P. D. Phelps, K. R. Stewart, C. P. Yakymyshyn, *Appl. Phys. Lett.* **1992**, *61*, 3080.
[89] T. J. Carrig, G. Rodriguez, T. Sharp Clement, A. J. Taylor, K. R. Stewart, *Appl. Phys. Lett.* **1995**, *66*, 10.
[90] T. Taniuchi, S. Okada, H. Nakanishi, *J. Appl. Phys.* **2004**, *95*, 5984.
[91] C. P. Hauri, C. Ruchert, C. Vicario, F. Ardana, *Appl. Phys. Lett.* **2011**, *99*, 161116.
[92] C. Vicario, M. Jazbinsek, A. V. Ovchinnikov, O. V. Chefonov, S. I. Ashitkov, M. B. Agranat, C. P. Hauri, *Opt. Express* **2015**, *23*, 4573.
[93] C. Vicario, A. V. Ovchinnikov, S. I. Ashitkov, M. B. Agranat, V. E. Fortov, C. P. Hauri, *Opt. Lett.* **2014**, *39*, 6632.
[94] C. Ruchert, C. Vicario, C. P. Hauri, *Opt. Lett.* **2012**, *37*, 899.
[95] A. Schneider, M. Neis, M. Stillhart, B. Ruiz, R. U. A. Khan, P. Günter, *J. Opt. Soc. Am. B* **2006**, *23*, 1822.
[96] C. Vicario, B. Monoszlai, M. Jazbinsek, S. H. Lee, O. P. Kwon, C. P. Hauri, *Sci. Rep.* **2015**, *5*, 14394.
[97] C. Vicario, B. Monoszlai, C. P. Hauri, *Phys. Rev. Lett.* **2014**, *112*, 213901.
[98] M. Shalaby, C. P. Hauri, *Nat. Commun.* **2015**, *6*, 5976.
[99] K. Reimann, *Rep. Prog. Phys.* **2007**, *70*, 1597.
[100] D. You, R. R. Jones, P. H. Bucksbaum, D. R. Dykaar, *Opt. Lett.* **1993**, *18*, 290.
[101] R. R. Jones, D. You, P. H. Bucksbaum, *Phys. Rev. Lett.* **1993**, *70*, 1236.
[102] X. Ropagnol, M. Khorasaninejad, M. Raeiszadeh, S. Safavi-Naeini, M. Bouvier, C. Y. Côté, A. Laramée, M. Reid, M. A. Gauthier, T. Ozaki, *Opt. Express* **2016**, *24*, 11299.
[103] X. Ropagnol, M. Bouvier, M. Reid, T. Ozaki, *J. Appl. Phys.* **2014**, *116*, 043107.
[104] A. Dreyhaupt, S. Winnerl, T. Dekorsy, M. Helm, *Appl. Phys. Lett.* **2005**, *86*, 121114.
[105] S. Preu, G. H. Döhler, S. Malzer, L. J. Wang, A. C. Gossard, *J. Appl. Phys.* **2011**, *109*, 061301.
[106] C. W. Berry, N. Wang, M. R. Hashemi, M. Unlu, M. Jarrahi, *Nat. Commun.* **2013**, *4*, 1622.
[107] N. Laman, D. Grischkowsky, *Appl. Phys. Lett.* **2008**, *93*, 051105.
[108] F. Kadlec, P. Kužel, J.-L. Coutaz, *Opt. Lett.* **2005**, *30*, 1402.
[109] G. H. Welsh, N. T. Hunt, K. Wynne, *Phys. Rev. Lett.* **2007**, *98*, 026803.
[110] G. K. P. Ramanandan, G. Ramakrishnan, N. Kumar, A. J. L. Adam, P. C. M. Planken, *J. Phys. D: Appl. Phys.* **2014**, *47*, 374003.
[111] T. Kampfrath, M. Battiato, P. Maldonado, G. Eilers, J. Nötzold, S. Mährlein, V. Zbarsky, F. Freimuth, Y. Mokrousov, S. Blügel, M. Wolf, I. Radu, P. M. Oppeneer, M. Münzenberg, *Nat. Nanotechnol.* **2013**, *8*, 256.
[112] T. Seifert, S. Jaiswal, U. Martens, J. Hannegan, L. Braun, P. Maldonado, F. Freimuth, A. Kronenberg, J. Henrizi, I. Radu, E. Beaurepaire, Y. Mokrousov, P. M. Oppeneer, M. Jourdan, G. Jakob, D. Turchinovich, L. M. Hayden, M. Wolf, M. Münzenberg, M. Kläui, T. Kampfrath, *Nat. Photonics* **2016**, *10*, 483.
[113] G. Torosyan, S. Keller, L. Scheuer, R. Beigang, E. T. Papaioannou, *Sci. Rep.* **2018**, *8*, 1311.
[114] M. T. Hibberd, D. S. Lake, N. A. B. Johansson, T. Thomson, S. P. Jamison, D. M. Graham, *Appl. Phys. Lett.* **2019**, *114*, 031101.
[115] T. S. Seifert, N. M. Tran, O. Gueckstock, S. M. Rouzegar, L. Nadvornik, S. Jaiswal, G. Jakob, V. V. Temnov, M. Münzenberg, M. Wolf, M. Kläui, T. Kampfrath, *J. Phys. D: Appl. Phys.* **2018**, *51*, 364003.
[116] R. L. Milot, M. T. Klug, C. L. Davies, Z. Wang, H. Kraus, H. J. Snaith, M. B. Johnston, L. M. Herz, *Adv. Mater.* **2018**, *30*, 1804506.
[117] C. L. Davies, J. Borchert, C. Q. Xia, R. L. Milot, H. Kraus, M. B. Johnston, L. M. Herz, *J. Phys. Chem. Lett.* **2018**, *9*, 4502.
[118] T. Seifert, S. Jaiswal, M. Sajadi, G. Jakob, S. Winnerl, M. Wolf, M. Kläui, T. Kampfrath, *Appl. Phys. Lett.* **2017**, *110*, 252402.
[119] A. Leitenstorfer, S. Hunsche, J. Shah, M. C. Nuss, W. H. Knox, *Appl. Phys. Lett.* **1999**, *74*, 1516.
[120] T. Kampfrath, J. Nötzold, M. Wolf, *Appl. Phys. Lett.* **2007**, *90*, 231113.
[121] P. T. Greenland, S. A. Lynch, A. F. G. van der Meer, B. N. Murdin, C. R. Pidgeon, B. Redlich, N. Q. Vinh, G. Aeppli, *Nature* **2010**, *465*, 1057.
[122] J. Savolainen, S. Ahmed, P. Hamm, *Proc. Natl. Acad. Sci. U. S. A.* **2013**, *110*, 20402.
[123] E. T. Papaioannou, G. Torosyan, S. Keller, L. Scheuer, M. Battiato, V. K. Mag-Usara, J. L'huillier, M. Tani, R. Beigang, *IEEE Trans. Magn.* **2018**, *54*, 1.
[124] R. I. Herapath, S. M. Hornett, T. S. Seifert, G. Jakob, M. Kläui, J. Bertolotti, T. Kampfrath, E. Hendry, *Appl. Phys. Lett.* **2019**, *114*, 041107.
[125] T. Seifert, U. Martens, S. Günther, M. A. W. Schoen, F. Radu, X. Z. Chen, I. Lucas, R. Ramos, M. H. Aguirre, P. A. Algarabel, A. Anadón, H. S. Körner, J. Walowski, C. Back, M. R. Ibarra, L. Morellón, E. Saitoh, M. Wolf, C. Song, K. Uchida, M. Münzenberg, I. Radu, T. Kampfrath, *SPIN* **2017**, *07*, 1740010.
[126] T. J. Huisman, C. Ciccarelli, A. Tsukamoto, R. V. Mikhaylovskiy, T. Rasing, A. V. Kimel, *Appl. Phys. Lett.* **2017**, *110*, 072402.
[127] Y. Sasaki, K. Z. Suzuki, S. Mizukami, *Appl. Phys. Lett.* **2017**, *111*, 102401.
[128] U. Nandi, M. S. Abdelaziz, S. Jaiswal, G. Jakob, O. Gueckstock, S. M. Rouzegar, T. S. Seifert, M. Kläui, T. Kampfrath, S. Preu, *Appl. Phys. Lett.* **2019**, *115*, 022405.
[129] H. Hamster, A. Sullivan, S. Gordon, W. White, R. W. Falcone, *Phys. Rev. Lett.* **1993**, *71*, 2725.
[130] T. Löffler, F. Jacob, H. G. Roskos, *Appl. Phys. Lett.* **2000**, *77*, 453.
[131] D. J. Cook, R. M. Hochstrasser, *Opt. Lett.* **2000**, *25*, 1210.
[132] V. Vaičaitis, O. Balachninaitė, U. Morgner, I. Babushkin, *J. Appl. Phys.* **2019**, *125*, 173103.
[133] M. Kress, T. Löffler, S. Eden, M. Thomson, H. G. Roskos, *Opt. Lett.* **2004**, *29*, 1120.
[134] X. Xie, J. Dai, X. C. Zhang, *Phys. Rev. Lett.* **2006**, *96*, 075005.
[135] K. Y. Kim, J. H. Glownia, A. J. Taylor, G. Rodriguez, *Opt. Express* **2007**, *15*, 4577.
[136] T. Bartel, P. Gaal, K. Reimann, M. Woerner, T. Elsaesser, *Opt. Lett.* **2005**, *30*, 2805.
[137] K. Y. Kim, A. J. Taylor, J. H. Glownia, G. Rodriguez, *Nat. Photonics* **2008**, *2*, 605.
[138] N. Karpowicz, X. Lu, X. C. Zhang, *J. Mod. Opt.* **2009**, *56*, 1137.
[139] V. A. Andreeva, O. G. Kosareva, N. A. Panov, D. E. Shipilo, P. M. Solyankin, M. N. Esaulkov, P. González de Alaiza Martínez, A. P. Shkurinov, V. A. Makarov, L. Bergé, S. L. Chin, *Phys. Rev. Lett.* **2016**, *116*, 063902.
[140] C. D'Amico, A. Houard, M. Franco, B. Prade, A. Mysyrowicz, A. Couairon, V. T. Tikhonchuk, *Phys. Rev. Lett.* **2007**, *98*, 235002.
[141] J. Dai, N. Karpowicz, X. C. Zhang, *Phys. Rev. Lett.* **2009**, *103*, 023001.
[142] G. Rodriguez, G. L. Dakovski, *Opt. Express* **2010**, *18*, 15130.
[143] M. D. Thomson, V. Blank, H. G. Roskos, *Opt. Express* **2010**, *18*, 23173.
[144] E. Matsubara, M. Nagai, M. Ashida, *Appl. Phys. Lett.* **2012**, *101*, 011105.
[145] T. I. Oh, Y. S. You, N. Jhajj, E. W. Rosenthal, H. M. Milchberg, K. Y. Kim, *New J. Phys.* **2013**, *15*, 075002.
[146] T. I. Oh, Y. J. Yoo, Y. S. You, K. Y. Kim, *Appl. Phys. Lett.* **2014**, *105*, 041103.

[147] M. Clerici, M. Peccianti, B. E. Schmidt, L. Caspani, M. Shalaby, M. Giguère, A. Lotti, A. Couairon, F. Légaré, T. Ozaki, D. Faccio, R. Morandotti, *Phys. Rev. Lett.* **2013**, *110*, 253901.
[148] V. Y. Fedorov, S. Tzortzakis, *Phys. Rev. A* **2018**, *97*, 063842.
[149] A. D. Koulouklidis, C. Gollner, V. Shumakova, V. Fedorov, A. Pugzlys, A. Baltuska, S. Tzortzakis, presented at *The European Conf. Lasers and Electro-Optics*, CLEO_Europe, Munich, Germany, June **2019**.
[150] V. Y. Fedorov, S. Tzortzakis, *Opt. Express* **2018**, *26*, 31150.
[151] A. Nguyen, K. J. Kaltenecker, J. C. Delagnes, B. Zhou, E. Cormier, N. Fedorov, R. Bouillaud, D. Descamps, I. Thiele, S. Skupin, P. U. Jepsen, L. Bergé, *Opt. Lett.* **2019**, *44*, 1488.
[152] Y. S. You, T. I. Oh, K. Y. Kim, *Phys. Rev. Lett.* **2012**, *109*, 183902.
[153] A. Gorodetsky, A. D. Koulouklidis, M. Massaouti, S. Tzortzakis, *Phys. Rev. A* **2014**, *89*, 033838.
[154] A. N. Tcypkin, E. A. Ponomareva, S. E. Putilin, S. V. Smirnov, S. A. Shtumpf, M. V. Melnik, E. Yiwen, S. A. Kozlov, X. C. Zhang, *Opt. Express* **2019**, *27*, 15485.
[155] L.-L. Zhang, W.-M. Wang, T. Wu, S.-J. Feng, K. Kang, C.-L. Zhang, Y. Zhang, Y.-T. Li, Z.-M. Sheng, X.-C. Zhang, *Phys. Rev. Appl.* **2019**, *12*, 014005.
[156] I. Dey, K. Jana, V. Y. Fedorov, A. D. Koulouklidis, A. Mondal, M. Shaikh, D. Sarkar, A. D. Lad, S. Tzortzakis, A. Couairon, G. R. Kumar, *Nat. Commun.* **2017**, *8*, 1184.
[157] A. Gopal, S. Herzer, A. Schmidt, P. Singh, A. Reinhard, W. Ziegler, D. Brömmel, A. Karmakar, P. Gibbon, U. Dillner, T. May, H. G. Meyer, G. G. Paulus, *Phys. Rev. Lett.* **2013**, *111*, 074802.
[158] G. Liao, Y. Li, H. Liu, G. G. Scott, D. Neely, Y. Zhang, B. Zhu, Z. Zhang, C. Armstrong, E. Zemaityte, P. Bradford, P. G. Huggard, D. R. Rusby, P. McKenna, C. M. Brenner, N. C. Woolsey, W. Wang, Z. Sheng, J. Zhang, *Proc. Natl. Acad. Sci. U. S. A.* **2019**, *116*, 3994.
[159] J. Liu, J. Dai, S. L. Chin, X. C. Zhang, *Nat. Photonics* **2010**, *4*, 627.
[160] B. Clough, J. Liu, X. C. Zhang, *Opt. Lett.* **2010**, *35*, 3544.
[161] I. Katayama, H. Aoki, J. Takeda, H. Shimosato, M. Ashida, R. Kinjo, I. Kawayama, M. Tonouchi, M. Nagai, K. Tanaka, *Phys. Rev. Lett.* **2012**, *108*, 097401.
[162] B. S. Dastrup, J. R. Hall, J. A. Johnson, *Appl. Phys. Lett.* **2017**, *110*, 162901.
[163] A. von Hoegen, R. Mankowsky, M. Fechner, M. Först, A. Cavalleri, *Nature* **2018**, *555*, 79.
[164] S. Maehrlein, A. Paarmann, M. Wolf, T. Kampfrath, *Phys. Rev. Lett.* **2017**, *119*, 127402.
[165] M. Sajadi, M. Wolf, T. Kampfrath, *Nat. Commun.* **2017**, *8*, 14963.
[166] P. Zalden, L. Song, X. Wu, H. Huang, F. Ahr, O. D. Mücke, J. Reichert, M. Thorwart, P. K. Mishra, R. Welsch, R. Santra, F. X. Kärtner, C. Bressler, *Nat. Commun.* **2018**, *9*, 2142.
[167] T. Kampfrath, R. K. Campen, M. Wolf, M. Sajadi, *J. Phys. Chem. Lett.* **2018**, *9*, 1279.
[168] W. Kuehn, P. Gaal, K. Reimann, M. Woerner, T. Elsaesser, R. Hey, *Phys. Rev. Lett.* **2010**, *104*, 146602.
[169] M. Hohenleutner, F. Langer, O. Schubert, M. Knorr, U. Huttner, S. W. Koch, M. Kira, R. Huber, *Nature* **2015**, *523*, 572.
[170] H. A. Hafez, S. Kovalev, J.-C. Deinert, Z. Mics, B. Green, N. Awari, M. Chen, S. Germanskiy, U. Lehnert, J. Teichert, Z. Wang, K.-J. Tielrooij, Z. Liu, Z. Chen, A. Narita, K. Müllen, M. Bonn, M. Gensch, D. Turchinovich, *Nature* **2018**, *561*, 507.
[171] R. Matsunaga, N. Tsuji, H. Fujita, A. Sugioka, K. Makise, Y. Uzawa, H. Terai, Z. Wang, H. Aoki, R. Shimano, *Science* **2014**, *345*, 1145.
[172] A. Dienst, M. C. Hoffmann, D. Fausti, J. C. Petersen, S. Pyon, T. Takayama, H. Takagi, A. Cavalleri, *Nat. Photonics* **2011**, *5*, 485.
[173] Y. Mukai, H. Hirori, T. Yamamoto, H. Kageyama, K. Tanaka, *New J. Phys.* **2016**, *18*, 013045.
[174] S. Baierl, M. Hohenleutner, T. Kampfrath, A. K. Zvezdin, A. V. Kimel, R. Huber, R. V. Mikhaylovskiy, *Nat. Photonics* **2016**, *10*, 715.
[175] S. Baierl, J. H. Mentink, M. Hohenleutner, L. Braun, T. M. Do, C. Lange, A. Sell, M. Fiebig, G. Woltersdorf, T. Kampfrath, R. Huber, *Phys. Rev. Lett.* **2016**, *117*, 197201.
[176] T. Elsaesser, K. Reimann, M. Woerner, Morgan & Claypool Publishers, San Rafael, CA, USA **2019**.
[177] J. Lu, X. Li, H. Y. Hwang, B. K. Ofori-Okai, T. Kurihara, T. Suemoto, K. A. Nelson, *Phys. Rev. Lett.* **2017**, *118*, 207204.
[178] W. Kuehn, K. Reimann, M. Woerner, T. Elsaesser, R. Hey, U. Schade, *Phys. Rev. Lett.* **2011**, *107*, 067401.
[179] H. Kim, J. Hunger, E. Cánovas, M. Karakus, Z. Mics, M. Grechko, D. Turchinovich, S. H. Parekh, M. Bonn, *Nat. Commun.* **2017**, *8*, 687.
[180] I. A. Finneran, R. Welsch, M. A. Allodi, T. F. Miller, G. A. Blake, *Proc. Natl. Acad. Sci. U. S. A.* **2016**, *113*, 6857.
[181] M. Liu, H. Y. Hwang, H. Tao, A. C. Strikwerda, K. Fan, G. R. Keiser, A. J. Sternbach, K. G. West, S. Kittiwatanakul, J. Lu, S. A. Wolf, F. G. Omenetto, X. Zhang, K. A. Nelson, R. D. Averitt, *Nature* **2012**, *487*, 345.
[182] M. Rini, R. A. Tobey, N. Dean, J. Itatani, Y. Tomioka, Y. Tokura, R. W. Schoenlein, A. Cavalleri, *Nature* **2007**, *449*, 72.
[183] X. Li, T. Qiu, J. Zhang, E. Baldini, J. Lu, A. M. Rappe, K. A. Nelson, *Science* **2019**, *364*, 1079.
[184] T. F. Nova, A. S. Disa, M. Fechner, A. Cavalleri, *Science* **2019**, *364*, 1075.
[185] M. Mitrano, A. Cantaluppi, D. Nicoletti, S. Kaiser, A. Perucchi, S. Lupi, P. Di Pietro, D. Pontiroli, M. Riccò, S. R. Clark, D. Jaksch, A. Cavalleri, *Nature* **2016**, *530*, 461.
[186] E. Balogh, K. Kovacs, P. Dombi, J. A. Fulop, G. Farkas, J. Hebling, V. Tosa, K. Varju, *Phys. Rev. A* **2011**, *84*, 023806.
[187] K. Kovács, E. Balogh, J. Hebling, V. Toşa, K. Varjú, *Phys. Rev. Lett.* **2012**, *108*, 193903.
[188] C. Lombosi, I. Márton, Z. Ollmann, J. Hebling, G. Farkas, P. Dombi, J. A. Fülöp, in *2015 European Conf. Lasers and Electro-Optics – European Quantum Electronics Conf.*, Optical Society of America, Munich **2015**.
[189] G. Herink, L. Wimmer, C. Ropers, *New J. Phys.* **2014**, *16*, 123005.
[190] K. Iwaszczuk, M. Zalkovskij, A. C. Strikwerda, P. U. Jepsen, *Optica* **2015**, *2*, 116.
[191] S. Li, R. R. Jones, *Nat. Commun.* **2016**, *7*, 13405.
[192] J. Hebling, J. A. Fülöp, M. I. Mechler, L. Pálfalvi, C. Tóke, G. Almási, *arXiv*:1109.6852, **2011**.
[193] Z. Tibai, M. Unferdorben, S. Turnár, A. Sharma, J. A. Fülöp, G. Almási, J. Hebling, *J. Phys. B: At., Mol. Opt. Phys.* **2018**, *51*, 134004.
[194] D. Zhang, A. Fallahi, M. Hemmer, X. Wu, M. Fakhari, Y. Hua, H. Cankaya, A.-L. Calendron, L. E. Zapata, N. Matlis, F. X. Kärtner, *Nat. Photonics* **2018**, *12*, 336.
[195] D. Zhang, A. Fallahi, M. Hemmer, H. Ye, M. Fakhari, Y. Hua, H. Cankaya, A.-L. Calendron, L. E. Zapata, N. H. Matlis, F. X. Kärtner, *Optica* **2019**, *6*, 872.
[196] W. R. Huang, E. A. Nanni, K. Ravi, K.-H. Hong, A. Fallahi, L. J. Wong, P. D. Keathley, L. E. Zapata, F. X. Kärtner, *Sci. Rep.* **2015**, *5*, 14899.
[197] W. Ronny Huang, A. Fallahi, X. Wu, H. Cankaya, A.-L. Calendron, K. Ravi, D. Zhang, E. A. Nanni, K.-H. Hong, F. X. Kärtner, *Optica* **2016**, *3*, 1209.
[198] D. A. Walsh, D. S. Lake, E. W. Snedden, M. J. Cliffe, D. M. Graham, S. P. Jamison, *Nat. Commun.* **2017**, *8*, 421.
[199] P. Baum, A. H. Zewail, *Proc. Natl. Acad. Sci. U. S. A.* **2006**, *103*, 16105.